

Tuning Fermilab Heavy Quarks in 2+1 Flavor Lattice QCD with Application to Hyperfine Splittings

C. Bernard,¹ C. DeTar,² M. Di Pierro,³ A.X. El-Khadra,⁴ R.T. Evans,^{4,5} E.D. Freeland,^{1,*}
E. Gámiz,^{4,6} Steven Gottlieb,^{7,8} U.M. Heller,⁹ J.E. Hetrick,¹⁰ A.S. Kronfeld,⁶ J. Laiho,^{1,11}
L. Levkova,² P.B. Mackenzie,⁶ J.N. Simone,⁶ R. Sugar,¹² D. Toussaint,¹³ and R.S. Van de Water¹⁴
(Fermilab Lattice and MILC Collaborations)

¹*Department of Physics, Washington University, St. Louis, Missouri 63130, USA*

²*Physics Department, University of Utah, Salt Lake City, Utah 84112, USA*

³*School of Computing, DePaul University, Chicago, Illinois 60604, USA*

⁴*Physics Department, University of Illinois, Urbana, Illinois 61801, USA*

⁵*Institut für Theoretische Physik, Universität Regensburg, 93040 Regensburg, Germany*

⁶*Fermi National Accelerator Laboratory, Batavia, Illinois 60510, USA*

⁷*Department of Physics, Indiana University, Bloomington, Indiana 47405, USA*

⁸*National Center for Supercomputing Applications, University of Illinois, Urbana 61801, Illinois, USA*

⁹*American Physical Society, One Research Road, Ridge, New York 11961, USA*

¹⁰*Physics Department, University of the Pacific, Stockton, California 95211, USA*

¹¹*Department of Physics and Astronomy, University of Glasgow, Glasgow, Scotland, UK*

¹²*Department of Physics, University of California, Santa Barbara, California 93106, USA*

¹³*Department of Physics, University of Arizona, Tucson, Arizona 85721, USA*

¹⁴*Physics Department, Brookhaven National Laboratory, Upton, New York 11973, USA*

(Dated: October 30, 2018)

We report the non-perturbative tuning of parameters— κ_c , κ_b , and κ_{crit} —that are related to the bare heavy-quark mass in the Fermilab action. This requires the computation of the masses of $D_s^{(*)}$ and $B_s^{(*)}$ mesons comprised of a Fermilab heavy quark and a staggered light quark. Additionally, we report the hyperfine splittings for $D_s^{(*)}$ and $B_s^{(*)}$ mesons as a cross-check of our simulation and analysis methods. We find a splitting of 145 ± 15 MeV for the D_s system and 40 ± 9 MeV for the B_s system. These are in good agreement with the Particle Data Group average values of 143.9 ± 0.4 MeV and 46.1 ± 1.5 MeV, respectively. The calculations are carried out with the MILC 2+1 flavor gauge configurations at three lattice spacings $a \approx 0.15, 0.12$ and 0.09 fm.

I. INTRODUCTION

Lattice QCD calculations play a critical role in the study of standard model physics and the search for new physics. For a set of lattice QCD calculations to be viable, several basic tasks are necessary. The bare gauge coupling must be eliminated in favor of an observable allowing the conversion from lattice to physical units; the bare masses in the lattice action must be tuned to correspond to physical quarks; and experimentally established quantities must be calculated in order to substantiate the method’s accuracy and reliability. Once these tasks are complete, a variety of quantities inaccessible to or not yet determined by experiment may be calculated, such as decay constants, form factors, and mass spectra.

The Fermilab Lattice and MILC Collaborations have reported several calculations [1–8] based on ensembles of lattice gauge fields with 2+1 flavors of sea quarks, generated by the MILC Collaboration [9, 10]. Details of the scale setting can be found in Refs. [11, 12], and details of the light-quark mass tuning in Ref. [11]. In this paper, we report on the necessary tuning of the heavy-quark action for charmed and bottom quarks. In particular, we describe calculations of the heavy-light pseudoscalar and vector meson masses using, for light quarks, the asqtad staggered action [13] and, for heavy quarks, the Fermilab interpretation [14] of the Sheikholeslami-Wohlert (“clover”) action [15] for Wilson fermions [16]. We use the spin-average of these meson masses to nonperturbatively tune the hopping parameter κ , which is equivalent to the bare heavy-quark mass. We also describe the determination of κ_{crit} , the value of κ for which a degenerate Wilson pseudoscalar’s mass vanishes. The value of κ_{crit} plays a minor role in the calculation of heavy-light matrix elements [3–5], and a more important role when determining a renormalized quark mass [6]. Finally, as a by-product of these calculations, we report the spin-dependent hyperfine splittings for B_s and D_s mesons, which test how well we have improved the chromomagnetic interaction.

Two aspects of the Fermilab method are important here. First, the Fermilab interpretation makes no assumptions about the size of the quark mass. Therefore, we are able to treat both charm and bottom quarks within the same framework. Second, since the Sheikholeslami-Wohlert action maintains the spin and flavor symmetries of heavy quarks, heavy-quark effective theory (HQET) can be used to interpret and improve lattice discretization effects [17, 18]. HQET techniques can be used to show

*eliz@fnal.gov

how the improvement works for observables, such as meson masses, in a way simpler than, though equivalent to, the Symanzik improvement program [19].

This paper is organized as follows. Section II reviews the theoretical framework upon which these calculations are based. Section III contains specific descriptions of the gauge configurations, actions, and operators used for the meson masses. Section IV covers the components of the numerical analysis. Section V details the fitting procedures. Section VI presents the results for the non-perturbative tuning of the heavy-quark hopping parameters κ_c and κ_b , the hyperfine splitting, and the critical hopping parameter κ_{crit} . Section VII summarizes with a discussion of improvements to these calculations that are currently underway. Details of the meson-mass discretization error estimation are given in Appendix A. Appendices B and C tabulate intermediate numerical results. The partially quenched chiral perturbation theory expression for the hyperfine splitting is derived in Appendix D.

II. THEORETICAL BACKGROUND

The hopping-parameter form of the heavy-quark action is [14]

$$S = S_0 + S_B + S_E, \quad (2.1)$$

where

$$S_0 = \sum_n \bar{\psi}_n \psi_n - \kappa \sum_{n,\mu} [\bar{\psi}_n (1 - \gamma_\mu) U_{n,\mu} \psi_{n+\hat{\mu}} + \bar{\psi}_{n+\hat{\mu}} (1 + \gamma_\mu) U_{n,\mu}^\dagger \psi_n], \quad (2.2)$$

$$S_B = \frac{i}{2} c_B \kappa \sum_{n;i,j,k} \epsilon_{ijk} \bar{\psi}_n \sigma_{ij} B_{n;k} \psi_n, \quad (2.3)$$

$$S_E = i c_E \kappa \sum_{n;i} \bar{\psi}_n \sigma_{0i} E_{n;i} \psi_n, \quad (2.4)$$

where $\sigma_{\mu\nu} = \frac{i}{2} [\gamma_\mu, \gamma_\nu]$. The chromomagnetic and chromoelectric fields $B_{n;i}$ and $E_{n;i}$ are standard and given in Ref. [14]. The term S_0 includes dimension-five terms to alleviate the fermion doubling problem [16]. The couplings c_E and c_B of the dimension-five operators in S_B and S_E are chosen to reduce discretization effects [14, 15].

The hopping parameter κ is related to the tadpole-improved bare quark mass by

$$am_0 = \frac{1}{u_0} \left(\frac{1}{2\kappa} - \frac{1}{2\kappa_{\text{crit}}} \right), \quad (2.5)$$

where a is the lattice spacing, u_0 is the tadpole-improvement factor [20], and κ_{crit} is the value of κ for which the pseudoscalar meson mass (of two degenerate Wilson quarks) vanishes. Our nonperturbative determination of κ_{crit} is discussed in Sec. VI C. To motivate our method of tuning κ , we first discuss the meson dispersion relation. We then turn to the HQET description of our Lagrangian to understand how to best use the dispersion relation.

The meson dispersion relation can be written, for $|\mathbf{p}| \ll m_0, a^{-1}$, as [14]

$$E(\mathbf{p}) = M_1 + \frac{\mathbf{p}^2}{2M_2} + O(\mathbf{p}^4). \quad (2.6)$$

Here, and throughout this work, we use lower-case m for quark masses and upper-case M for meson masses. M_1 and M_2 are known as the rest mass and kinetic mass, respectively. Because the lattice breaks Lorentz invariance, $M_1 \neq M_2$, although $M_1 \rightarrow M_2$ as $a \rightarrow 0$ for the action in Eq. (2.1). By tuning κ , one could adjust the bare, heavy-quark mass such that *either* M_1 or M_2 is equal to the physical meson mass. (To set $M_1 = M_2$ requires the introduction, and tuning, of an additional parameter in the action. This is possible but, as discussed below, not necessary [14].)

To clarify the role of the different masses in Eq. (2.6), it is useful to introduce an effective Lagrangian. This also sets up a language for discussing discretization errors later. Because the action in Eq. (2.1) has the same heavy-quark spin and flavor symmetries as continuum QCD, HQET is an obvious candidate for its description [17, 18]. To employ HQET, one separates the short-distance physics at the scale of the inverse heavy-quark mass $1/m_Q$ from the long-distance physics at the characteristic scale of QCD, Λ_{QCD} . The fact that we have a lattice does not change the validity or utility of this separation. It simply means that the lattice spacing a must be included in the description of the short-distance physics. Thus, the short-distance coefficients of HQET applied to Eq. (2.1) differ from those arrived at by applying HQET to continuum QCD; these differences are the heavy-quark discretization errors. Parameters in the lattice action can be chosen to minimize them.

We introduce the heavy-quark effective Lagrangian for our lattice gauge theory by writing [17, 18]

$$\mathcal{L}_{\text{LGT}} \doteq \mathcal{L}_{\text{light}} + \mathcal{L}_{\text{HQET}}, \quad (2.7)$$

where $\mathcal{L}_{\text{light}}$ is the Symanzik local effective Lagrangian for the light degrees of freedom and \doteq means the Lagrangian on the right-hand side describes the on-shell matrix elements of the Lagrangian on the left-hand side. The HQET Lagrangian has a power-counting scheme, denoted by

$$\mathcal{L}_{\text{HQET}} = \sum_s \mathcal{L}_{\text{HQET}}^{(s)}, \quad (2.8)$$

where $\mathcal{L}_{\text{HQET}}^{(s)}$ includes all operators of dimension $4 + s$, with coefficients of dimension $-s$ consisting of powers of the short distances, $1/m_Q$ or a . The first few terms in $\mathcal{L}_{\text{HQET}}$ are [17]

$$\mathcal{L}_{\text{HQET}}^{(0)} = -\bar{h}^{(+)}(D_4 + m_1)h^{(+)}, \quad (2.9)$$

$$\mathcal{L}_{\text{HQET}}^{(1)} = \bar{h}^{(+)} \frac{\mathbf{D}^2}{2m_2} h^{(+)} + \bar{h}^{(+)} \frac{i\boldsymbol{\sigma} \cdot \mathbf{B}}{2m_B} h^{(+)}, \quad (2.10)$$

$$\mathcal{L}_{\text{HQET}}^{(2)} = \bar{h}^{(+)} \frac{i\boldsymbol{\sigma} \cdot (\mathbf{D} \times \mathbf{E})}{8m_E^2} h^{(+)} + \bar{h}^{(+)} \frac{\mathbf{D} \cdot \mathbf{E}}{8m_D^2} h^{(+)}, \quad (2.11)$$

where $h^{(+)}$ is a two-component heavy-quark field, $\boldsymbol{\sigma}$ are the Pauli matrices, and \mathbf{B} and \mathbf{E} are the continuum gauge fields. The masses m_1, m_2, m_B, m_E , and m_D are functions of the bare-quark mass m_0 and the gauge coupling. For example, the masses m_1 and m_2 are defined to all orders in perturbation theory by Eq. (2.6), applied now to the pole energy of a one-quark state [21]. The entries in Eqs. (2.9)–(2.11) are commonly referred to as follows. $\mathcal{L}_{\text{HQET}}^{(0)}$ gives the rest mass. The first term of $\mathcal{L}_{\text{HQET}}^{(1)}$ is the kinetic energy and the second is the chromomagnetic, or hyperfine, interaction. The first term of $\mathcal{L}_{\text{HQET}}^{(2)}$ is the spin-orbit interaction while the second is known as the Darwin term.

For the pseudoscalar and vector meson rest masses, the HQET formalism can be used to show that [17]

$$M_1^{(*)} = m_1 + \bar{\Lambda}_{\text{lat}} - \frac{\lambda_{1,\text{lat}}}{2m_2} - d_J \frac{\lambda_{2,\text{lat}}}{2m_B} + O(1/m^2), \quad (2.12)$$

where J is the total meson angular momentum with $d_0 = 3$ and $d_1 = -1$ for the pseudoscalar (M_1) and vector (M_1^*) mesons, respectively. The quantities $\bar{\Lambda}_{\text{lat}}$, $\lambda_{1,\text{lat}}$, and $\lambda_{2,\text{lat}}$ are HQET matrix elements. At non-zero lattice spacing they contain discretization effects from $\mathcal{L}_{\text{light}}$, hence the subscript “lat”. The continuum limit of these quantities yields their counterparts in HQET applied to continuum QCD [17], which provides a basis for computing the continuum-QCD quantities $\bar{\Lambda}$ and λ_1 [22].

Mass splittings and matrix elements such as decay constants and form factors are not affected by the value of m_1 [17]. Thus, Eqs. (2.9) and (2.10) show that the kinetic mass m_2 is the first mass in the expansion that does play a role in the dynamics. We therefore would like to associate m_2 , and hence M_2 , with the physical mass, tolerating $m_1 \neq m_2$ (and $M_1 \neq M_2$) for nonzero lattice spacings. The nonperturbative tuning of κ then entails adjusting κ until the meson kinetic mass—determined by fits of Monte Carlo lattice data to the dispersion relation, Eq. (2.6)—equals that of the physical meson mass. A relation similar to Eq. (2.12) holds for M_2

$$M_2^{(*)} = m_2 + \bar{\Lambda}_{\text{lat}} + O(1/m), \quad (2.13)$$

with the leading discretization errors appearing in the $1/m$ contribution. Final values for the nonperturbative tuning of κ are given in Sec. VI A.

To calculate the hyperfine splitting of the D_s or B_s meson, consider

$$\Delta_1 \equiv M_1^* - M_1. \quad (2.14)$$

From Eq. (2.12),

$$M_1^* - M_1 = 4 \frac{\lambda_{2,\text{lat}}}{2m_B} + \dots, \quad (2.15)$$

which differs from the continuum splitting only by discretization errors in the light quarks and gluons appearing in $\lambda_{2,\text{lat}}$, the mismatch of m_B and its continuum counterpart (or, equivalently, the choice of c_B), and similar contributions from higher-dimension operators [17, 23]. The splitting of kinetic masses, $\Delta_2 \equiv M_2^* - M_2$, does not depend on m_B ; rather, it depends on

other generalized masses which are not tuned in our simulations.¹ Thus, Δ_1 formally has smaller discretization errors than Δ_2 . Δ_1 is also statistically cleaner than Δ_2 . In Eq. (2.15), $1/m_B$ is sensitive to the clover coupling c_B in Eq. (2.3), so Δ_1 tests how well it has been chosen. The B_s and D_s hyperfine splittings are given in Sec. VI B.

III. SIMULATIONS

In this section, we describe the gauge configurations used and the details of the actions, operators, and correlation functions that describe the heavy-light mesons. In Section III A, we discuss the gauge configurations and the parameters that describe each ensemble. We also review how the lattice spacing is determined and the values of the conversion factors r_1 and r_1/a . In Section III B, we discuss parameter choices for the valence quarks and the smearing of the heavy-quark wave function and how correlators are built from heavy and light quark fields.

A. Gauge Configurations and Related Parameters

We use the MILC gauge configurations [9, 10] that have 2+1 flavors of asqtad-improved staggered sea quarks [13] and a Symanzik-improved gluon action [24, 25]. Discretization errors from the sea quarks and gluons start at $O(\alpha_s a^2, a^4)$. The four-fold degeneracy of staggered sea quarks is removed by taking the fourth root of the determinant. To support the legitimacy of this procedure, Shamir has developed a renormalization-group framework for lattice QCD with staggered fermions, which he uses to argue that non-local effects of the rooted staggered theory are absent in the continuum limit [26]. Additional support for this procedure comes from chiral perturbation theory arguments [27, 28]. Reviews of these papers and of other evidence that this procedure reproduces the correct continuum limit appear in [11, 29, 30].

Table I lists the parameters of the gauge configurations used in this work. All configurations have been gauge-fixed to Coulomb gauge. Ensembles of configurations are grouped by their approximate lattice spacing and are referred to as “fine” ($a \approx 0.09$ fm), “coarse” ($a \approx 0.12$ fm), and “medium-coarse” ($a \approx 0.15$ fm). The simulation bare masses of the light and strange sea quarks are denoted by am'_l and am'_s , respectively, where am'_l is the mass of the two lighter sea-quarks. The range of am'_l is light enough that the physical up- and down-quark masses can be reached by a chiral extrapolation, while am'_s is close to the physical strange-quark mass. For convenience below, we write (am'_l, am'_s) to identify ensembles, e.g., “the (0.0031, 0.031) fine ensemble”. Also in Table I are the tadpole factors u_0 [20, 31], determined from the mean plaquette and used to improve the gauge-configuration actions [9, 10]. The value of the physical strange-quark mass is denoted by the unprimed m_s [31].

To convert between lattice and physical units, the physical value of the lattice spacing must be determined. We define the distance r_1 [12] by

$$r_1^2 F(r_1) = 1, \quad (3.1)$$

where $F(r)$ is the force between static quarks, calculated on the lattice. For each ensemble, this yields a value of r_1 in lattice units, r_1/a . The values are then “smoothed” by fitting $\ln(r_1/a)$, from all ensembles, to a polynomial in β and $2am'_l + am'_s$ [31]. The physical value of r_1 is obtained via the lattice calculation of an experimentally measurable quantity. We consider two current determinations here. One uses a lattice calculation of the $\Upsilon(2S)$ - $\Upsilon(1S)$ splitting [33] to arrive at $r_1 = 0.318(7)$ fm [10, 34]. A more recent determination using $r_1 f_\pi$ gives $r_1 = 0.3108(15)_{(-79)}^{(+26)}$ fm [35]. These two determinations are consistent within errors. Because the determination of r_1 from f_π uses finer lattice spacings, we take that value,

$$r_1 = 0.3108_{(-80)}^{(+30)} \text{ fm} \quad (3.2)$$

with no additional error. While this work was being completed, a new determination of r_1 that uses two mass splittings and one decay constant became available; $r_1 = 0.3133_{(-3)}^{(+23)}$ [36], which is consistent with the value used in this work. Quantities can now be converted from lattice to physical units by using r_1 and the appropriate value of r_1/a given in Table I [31].

B. Meson Correlation Functions

Table II lists the values of parameters used in the valence-quark actions. For the light valence quark, we again use the asqtad action [13] and masses am'_q close to the physical value of the strange-quark mass, cf. Table I. From Eqs. (2.9)–(2.11), one can

¹ Tree-level expressions for these masses, and hence their mismatch, can be found in Ref. [23].

TABLE I: Parameters describing the ensembles used. The dimensions of the lattice are given in terms of the spatial (N_L) and temporal (N_T) size in lattice units. The gauge coupling is given by $\beta = 10/g^2$. The bare masses of the light and strange sea quarks are given by am'_l and am'_s , respectively. $L = aN_L$ is the linear spatial dimension of the lattice in fm. The column labeled N_{cf} is the number of configurations used in this work. The plaquette-determined tadpole-improvement factor is u_0 [31]. The physical strange quark mass is am_s [31] with errors, statistical and systematic, of less than one percent. The ratio r_1/a is described in the text; errors are Hessian from the smoothing fit. The final column lists the value of the inverse lattice spacing a^{-1} using $r_1 = 0.3108^{(+30)}_{(-80)}$ fm to convert from r_1/a ; errors are from the error on r_1 and r_1/a .

	$N_L^3 \times N_T$	β	am'_l	am'_s	L (fm)	N_{cf}	u_0	am_s	r_1/a	a^{-1} GeV
“Fine” $a \approx 0.09$ fm	$40^3 \times 96$	7.08	0.0031	0.031	3.5	435	0.8779	0.0252	3.692(6)	2.344^{+60}_{-23}
	$28^3 \times 96$	7.09	0.0062	0.031	2.4	557	0.8782	0.0252	3.701(5)	2.349^{+61}_{-23}
	$28^3 \times 96$	7.11	0.0124	0.031	2.4	518	0.8788	0.0252	3.721(5)	2.362^{+61}_{-23}
“Coarse” $a \approx 0.12$ fm	$24^3 \times 64$	6.76	0.005	0.05	2.9	529	0.8678	0.0344	2.645(3)	1.679^{+43}_{-16}
	$20^3 \times 64$	6.76	0.007	0.05	2.4	836	0.8678	0.0344	2.635(3)	1.672^{+43}_{-16}
	$20^3 \times 64$	6.76	0.010	0.05	2.4	592	0.8677	0.0344	2.619(3)	1.663^{+43}_{-16}
	$20^3 \times 64$	6.79	0.020	0.05	2.4	460	0.8688	0.0344	2.651(3)	1.683^{+43}_{-16}
	$20^3 \times 64$	6.81	0.030	0.05	2.4	549	0.8696	0.0344	2.657(4)	1.687^{+43}_{-16}
“Medium-coarse” $a \approx 0.15$ fm	$16^3 \times 48$	6.572	0.0097	0.0484	2.4	631	0.8604	0.0426	2.140(4)	1.358^{+35}_{-13}
	$16^3 \times 48$	6.586	0.0194	0.0484	2.4	631	0.8609	0.0426	2.129(3)	1.352^{+35}_{-13}
	$16^3 \times 48$	6.600	0.0290	0.0484	2.4	440	0.8614	0.0426	2.126(3)	1.350^{+35}_{-13}

see that with m_2 tuned to the physical mass, the leading mismatch between lattice and continuum physics is in the hyperfine term in $\mathcal{L}_{\text{HQET}}^{(1)}$. In principle, one can tune m_B to its continuum counterpart yielding a match between lattice and continuum actions for both terms in Eq. (2.10). Here, we use the tree-level expression for m_B , which leaves the leading mismatch at $O(\alpha_s a \Lambda)$. By setting $c_E = c_B$ we obtain the Sheikholeslami-Wohlert, $O(a)$ -improvement of discretization errors in the action [15]. From the HQET perspective, this leaves $m_E \neq m_2$ in Eq. (2.11), but the effects of this mistuning are at $O(a^2 \Lambda^2)$ and $O(\alpha_s a \Lambda^2/m_Q)$. Implementing the improvements above and using tree-level tadpole improvement in the perturbative expressions [20, 24], we use $c_E = c_B = u_0^{-3}$.

The values of u_0 used in the heavy-quark and light-valence actions are given in Table II. For the fine and medium-coarse ensembles, they are the plaquette values used to generate the MILC gauge configurations. For the coarse ensembles, the Landau-gauge link value was used. The use of different u_0 definitions results in a slight mismatch between the light valence- and sea-quark actions. In part because the meson mass is relatively insensitive to the strange sea-quark mass, we do not expect any significant systematic errors from this mismatch. Changes in u_0 result in changes to the bare mass of the heavy quark as well, but this effect is partly absorbed by the nonperturbative tuning of κ and κ_{crit} . Table II also lists the nominal values of the light valence-quark mass and sets of κ values for bottom and charm mesons. These sets of κ values, and mesons created from them, are referred to as charm-type or bottom-type.

With the parameters of the actions set, we now turn to the construction of the two-point correlators. Contributions from excited states can be significantly reduced by using a spatially smeared source, sink, or both, for the heavy-quark propagator. For the correlators in this work, we use two types of source-sink combinations for the heavy quarks. One is simply a delta function for both the source and sink; we refer to this as the local correlator. The other smears the field $\psi(t, \mathbf{x})$ with a discretized version [37] of the $1S$ charmonium wavefunction, $S(\mathbf{y})$, based on the Richardson potential [38]:

$$\phi(t, \mathbf{x}) = \sum_{\mathbf{y}} S(\mathbf{y}) \psi(t, \mathbf{x} + \mathbf{y}), \quad (3.3)$$

and the smearing wavefunction is applied after fixing to Coulomb gauge. Correlators using $\phi(t, \mathbf{x})$ are referred to as smeared correlators. All light valence quarks have a local source and sink. The meson correlator is

$$C_{i,j}(t, \mathbf{p}) = \sum_{\mathbf{x}} \langle \mathcal{O}_j^\dagger(t, \mathbf{x}) \mathcal{O}_i(0, \mathbf{0}) \rangle e^{i\mathbf{p} \cdot \mathbf{x}}, \quad (3.4)$$

where i, j denote the source, sink smearing of the heavy-quark field; for this work $i = j$. $\mathcal{O}_i(t, \mathbf{x})$ is a bilinear interpolating operator with a gamma-matrix structure that yields quantum numbers appropriate for either pseudoscalar or vector mesons. To construct this operator, we combine a one-component, staggered light-quark spinor with a four-component, Wilson-type heavy-quark spinor in a manner similar to Ref. [39],

$$\mathcal{O}_\Xi(t, \mathbf{x}) = \bar{\psi}_\alpha(t, \mathbf{x}) \Gamma_{\alpha\beta} \Omega_{\beta\Xi}(t, \mathbf{x}) \chi(t, \mathbf{x}), \quad (3.5)$$

where $\Gamma = \gamma_5$ or γ_μ ; α, β are spin indices; and $\Omega(x) \equiv \gamma_1^{x_1} \gamma_2^{x_2} \gamma_3^{x_3} \gamma_4^{x_4}$. The fields $\bar{\psi}$ and χ are the Wilson-type and staggered fields, respectively, and the smeared correlator is constructed in the same way, but with $\bar{\phi}$ instead of $\bar{\psi}$. The transformation

TABLE II: Parameters used in the valence-quark actions. The bare masses of the light and strange sea quarks (am'_l, am'_s) label the ensemble. The mass of the light (staggered) valence quark is given by am'_q . c_E and c_B are the coefficients of the chromoelectric and chromomagnetic contributions to the Lagrangian. With $c_E = c_B$, they are the usual Sheikholeslami-Wohlert coupling. u_0 is the tadpole-improvement factor from measurements of the average plaquette for the fine and medium-coarse ensembles and from the Landau-gauge link on the coarse ensembles. Hopping parameter values κ used for bottom-like and charm-like heavy quarks are given in the final two columns.

Lattice	(am'_l, am'_s)	am'_q	$c_E = c_B$	u_0	bottom-type κ	charm-type κ
Fine	(0.0031, 0.031)	0.0272, 0.031	1.478	0.8779	0.0923	0.127
	(0.0062, 0.031)	0.0272, 0.031	1.476	0.8782	0.090, 0.0923, 0.093	0.1256, 0.127
	(0.0124, 0.031)	0.0272, 0.031	1.473	0.8788	0.0923	0.127
Coarse	(0.005, 0.050)	0.030, 0.0415	1.72	0.836	0.086	0.122
	(0.007, 0.050)	0.030, 0.0415	1.72	0.836	0.074, 0.086, 0.093	0.119, 0.122, 0.124
	(0.010, 0.050)	0.030, 0.0415	1.72	0.8346	0.074, 0.086, 0.093	0.119, 0.122, 0.124
	(0.020, 0.050)	0.030, 0.0415	1.72	0.8369	0.074, 0.086, 0.093	0.122, 0.124
	(0.030, 0.050)	0.030, 0.0415	1.72	0.8378	0.086	0.122
Medium-coarse	(0.0097, 0.0484)	0.0387, 0.0484	1.570	0.8604	0.070, 0.080	0.115, 0.122 ^a , 0.125
	(0.0194, 0.0484)	0.0387, 0.0484	1.567	0.8609	0.070, 0.076, 0.080	0.115, 0.122, 0.125
	(0.0290, 0.0484)	0.0484	1.565	0.8614	0.070, 0.080	0.115, 0.125

^aUsed only with $am'_q = 0.484$.

properties of $\mathcal{O}_\Xi(x)$ under shifts by one lattice spacing are such that Ξ can be viewed as playing the role of the (fermionic) taste index [30, 40]. In our correlation functions, $\mathcal{O}_\Xi(x)$ is summed over 2^4 hypercubes, and so Ξ can be interpreted as a taste degree of freedom in the sense of Refs. [41, 42].

IV. ANALYSIS OVERVIEW

In this section, we describe the components of our analysis. Section IV A discusses the two-point correlator fits used to determine the meson energies $aE(\mathbf{p})$. Section IV B describes how we fit the meson dispersion relation to obtain M_2 . Finally, Sec. IV C explains how κ is tuned and how the hyperfine splitting is determined.

A. Two-point Correlator Fits: $E(\mathbf{p})$

To determine $E(\mathbf{p})$, we simultaneously fit the local and smeared heavy-light-meson two-point correlators to the function

$$C_{i,i}(t, \mathbf{p}) = \sum_{\eta=0}^{N-1} \left[Z_{i,\eta}^2 \left(e^{-E_\eta(\mathbf{p})t} + e^{-E_\eta(\mathbf{p})(N_T-t)} \right) + (-1)^{t+1} (Z_{i,\eta}^p)^2 \left(e^{-E_\eta^p(\mathbf{p})t} + e^{-E_\eta^p(\mathbf{p})(N_T-t)} \right) \right], \quad (4.1)$$

where N_T is the temporal extent of the lattice, and terms proportional to $e^{-E_\eta(\mathbf{p})(N_T-t)}$ are due to periodic boundary conditions. To simplify notation in this subsection, the lattice spacing a is not written out explicitly. Correlation functions containing staggered light quarks have contributions from both desired- and opposite-parity states with the opposite-parity states having the temporally-oscillating prefactor $(-1)^{t+1}$ [39]. We take each energy level η in Eq. (4.1) to include a pair of states consisting of one desired- and one opposite-parity state; the number of pairs of states in a fit is given by N . Quantities associated with the tower of opposite-parity states are denoted by the superscript “p.”

Equation (4.1) contains $2N$ exponentials, and the number of time slices in our data set is finite. Although it is straightforward to separate the two different parities—because of the $(-1)^{t+1}$ —it is difficult to separate states within each tower. Rather than relying solely on taking t large enough, we use the technique of constrained curve fitting [39, 43, 44]. We thus minimize an augmented χ^2 [43],

$$\chi_{\text{aug}}^2 \equiv \chi^2 + \sum_k \frac{(P_k - \tilde{P}_k)^2}{\sigma_{\tilde{P}_k}^2}, \quad (4.2)$$

which means each fit parameter P_k is provided a prior Gaussian probability distribution function with central value and width $(\tilde{P}_k, \sigma_{\tilde{P}_k})$. The central value for fitted quantities comes from minimizing χ_{aug}^2 on the whole ensemble. We take the parameters to be $E_0^{(p)}$, $\ln(Z_{i,\eta}^{(p)})$, and (for $\eta > 0$) $\ln(\Delta E_\eta^{(p)})$, where $\Delta E_\eta^{(p)} = E_\eta^{(p)} - E_{\eta-1}^{(p)}$, thereby enforcing a tower of states with increasing energy.

In general, one considers a quantity to be determined by the data only if the statistical error, discussed next, is smaller than the corresponding prior width. In this work, we are most concerned with the lowest-lying desired parity state, and the data—not the priors—always determine E_0 and $Z_{i,0}$. For parameters that are poorly constrained by the data, such as those describing excited states, these priors prevent the fitter from searching fruitlessly along flat directions in parameter space. Because of the freedom in choosing the prior, we test whether the ground-state results are prior-independent, and stable. When testing the stability of fit results, we use the Hessian error, defined as

$$\sigma_{P_i} = \sqrt{2 \left(\frac{\partial^2 \chi_{\text{aug}}^2}{\partial P_i \partial P_j} \right)_{ii}^{-1}}, \quad (4.3)$$

because its straightforward definition allows it to be quickly calculated for a single fit.

When using χ_{aug}^2 to measure the goodness of fit, we count the degrees of freedom as the number of data points; the number of fit parameters is not subtracted since there are an equal number of extra terms in χ_{aug}^2 . In some cases, this could result in misleadingly low values of $\chi_{\text{aug}}^2/\text{dof}$. For example, if the prior width $\sigma_{\tilde{P}_k}$ is much larger than $(P_k - \tilde{P}_k)$, the associated term in χ_{aug}^2 will be much smaller than the others. This could be adjusted *a posteriori* by reducing the degrees of freedom, but it would require devising a criterion for “large $\sigma_{\tilde{P}_k}$ ”. We do not make such adjustments in our analyses. Instead, to determine goodness of fit, we monitor the values of $\chi_{\text{aug}}^2/\text{dof}$ from constrained fits, but rely equally on the stability of fit results.

We estimate statistical uncertainties by generating pseudo-ensembles via the bootstrap method. When fitting a pseudo-ensemble, the central value of each prior is drawn randomly from its Gaussian probability distribution while the prior width is kept the same [39, 43]. To prevent large, simultaneous but uncorrelated fluctuations among prior central values, which could destabilize a fit, we restrict the randomized prior central values to $\pm 1.5\sigma_{\tilde{P}}$. Final errors quoted for meson energies and functions thereof, such as the spin-averaged mass, are obtained from their bootstrap distributions. We define the upper (lower) 68%-distribution point as the value at which 16% of the distribution has a higher (lower) value. We refer to half of the distance between these two points as the average 68% bootstrap error.

B. Dispersion Relation Fits: The Kinetic Mass

Having determined $E(\mathbf{p})$, we use the dispersion relation to determine the kinetic meson mass, which we then use to tune the hopping parameter κ . The low-momentum expansion for $E(\mathbf{p})$ is

$$E(\mathbf{p}) = M_1 + \frac{\mathbf{p}^2}{2M_2} - \frac{a^3 W_4}{6} \sum_i p_i^4 - \frac{(\mathbf{p}^2)^2}{8M_4^3} + \dots, \quad (4.4)$$

where W_4 and the deviation of M_4 from M_2 capture lattice artifacts. (In the continuum limit $a^3 W_4 = 0$ and $M_4 = M_2$.) The vector \mathbf{n} is defined by

$$a\mathbf{p} = (2\pi/N_L) \mathbf{n}, \quad (4.5)$$

where N_L is the spatial extent of the lattice, given in Table I; data are generated for $|\mathbf{n}| \leq 3$. Noise in $E(\mathbf{p})$ increases with increasing momentum, though, and is substantial by the time $O(\mathbf{p}^4)$ effects become significant. For charm-type mesons, squaring the energy yields a substantial cancellation in the $O(\mathbf{p}^4)$ contribution because $aM_1 \approx aM_2 \approx aM_4$. While this is not true for bottom-type mesons, the mass of these mesons is large enough to cause suppression via the $1/M$ factors whether $E(\mathbf{p})$ or $E^2(\mathbf{p})$ is used. By fitting to $E^2(\mathbf{p})$ then, the contributions from $O(\mathbf{p}^4)$ effects are reduced, and we are able to do a linear fit to low-momentum data, $|\mathbf{n}| \leq 2$. Setting $M_1 = E(\mathbf{0})$ from the zero-momentum correlator, we square Eq. (4.4) and fit

$$E^2(\mathbf{p}) - M_1^2 = C\mathbf{p}^2 \quad (4.6)$$

to obtain C . Finally, we set $M_2 = M_1/C$. The largest \mathbf{p} is chosen so that the $O(\mathbf{p}^4)$ effects are expected to be negligible, based on tree-level values of the analogous quark quantities w_4 and $1/m_4^3$. We confirm the negligibility of these terms by inspecting plots of the data and monitoring χ^2/dof . (We do not use constrained curve fitting here and so we minimize the usual χ^2 .) This procedure is repeated for each bootstrap-generated pseudo-ensemble, yielding bootstrap distributions for aM_1 and aM_2 .

C. The Hopping Parameter κ and the Hyperfine Splitting Δ_1

For tuning κ , it is helpful to remove the leading discretization errors from spin-dependent terms. Let the spin-averaged kinetic meson mass be

$$\overline{M}_2 = \frac{1}{4}(M_2 + 3M_2^*), \quad (4.7)$$

where M_2 and M_2^* are determined as described in Sec. IV B. This leaves the second, spin-independent term in Eq. (2.11) as the leading source of discretization error at $O(a^2\Lambda^2)$. Our goal then is to determine the value of κ that will result in a value of \overline{M}_2 that agrees with the experimental value taken from the Particle Data Group (PDG).

For each lattice spacing, we use the following procedure to tune κ . Using three or more ensembles, we study the light sea-quark mass dependence of $a\overline{M}_2$ for at least one combination of κ and m'_q . This gives us some insight into the behavior of $a\overline{M}_2$ in the physical–sea-quark–mass limit and allows us to assign an uncertainty to $a\overline{M}_2$ due to non-physical sea-quark masses. Next, on at least one ensemble, we determine $a\overline{M}_2$ at two staggered, valence-quark masses near the strange-quark mass. This allows us to determine the dependence of $a\overline{M}_2$ on the staggered, valence-quark mass and interpolate linearly to the physical value if no simulated mass is close enough to the tuned strange-quark mass. Having dealt with the staggered-valence and light sea-quark masses, we take $a\overline{M}_2$ at the physical, strange valence-quark mass at two values of κ and interpolate linearly in κ to the spin-averaged value of the meson masses, given by the Particle Data Group (PDG) [45], converted to lattice units with a from Table I. Finally, we combine the uncertainties in the tuned value of κ from statistical and discretization errors in the meson mass, staggered-valence mass mistuning, non-physical sea-quark masses, and errors from the lattice-spacing conversion of the PDG mass.

To determine the hyperfine splitting, we start with the results for $M_1 = E(\mathbf{0})$. For each lattice spacing, we use values of $a\Delta_1$ at, or linearly interpolated to, the tuned charm and bottom κ values. We then consider uncertainties from statistics, the tuning of κ and am_s , non-physical sea-quark masses, and discretization. The value of $a\Delta_1$ on the fine lattice is taken as our central value and results on the coarse and medium coarse lattices are used in the error analysis. In the final value, we also include an uncertainty due to the conversion to physical units.

V. FITTING DETAILS FOR $E(\mathbf{p})$, M_1 , M_2

In this section, we describe the details of our fitting procedure for the meson energy $E(\mathbf{p})$ and the meson rest and kinetic masses, M_1 and M_2 . Our objective here is to document thoroughly our fitting procedures, including values for the priors, and tests. Readers who are more interested in a summary can skip to Sec. V C.

Section V A discusses the parameters used in our two-point correlator fits for $E(\mathbf{p})$ (Sec. V A 1) and the evaluation of goodness of fit via $\chi_{\text{aug}}^2/\text{dof}$ and tests of stability (Sec. V A 2). In most tests discussed here, Hessian errors were used, because they are fast and straightforward. Our complete data set, exhibited in Table II, contains several ensembles at each of the three lattice spacings. As explained in Sec. V A 1, one ensemble at each lattice spacing is chosen for the purpose of setting priors in Eq. (4.2). For tuning κ , we need data over a range of κ and am'_q on a fixed ensemble. At the fine lattice spacing, such data were generated on only one ensemble, (0.0062, 0.031), so we set priors and tune κ on that same ensemble. For the coarse and medium-coarse lattice spacings, we have data for a range of κ and am'_q on several ensembles. We take the coarse (0.010, 0.050), and medium-coarse (0.0194, 0.0484) ensembles to set priors and then the ensembles with the smallest am'_l (and a range of κ and am'_q) to tune κ . We compute the hyperfine splittings from the same ensembles on which κ was tuned. These choices are summarized in Table III. Data from other ensembles listed in Table II are used to estimate uncertainties.

Fits of the dispersion relation to determine M_2 from $E(\mathbf{p})$ are comparatively simple, and Sec. V B provides details that may be of interest.

A. Two-point fits: $E(\mathbf{p})$, M_1

The number of gauge configurations in each ensemble is given in Table I. To improve statistics, we generate data at four time sources on each of the fine and coarse gauge configurations and at eight time sources for medium-coarse configurations. We also average the correlator points $C(t)$ and $C(N_T - t)$. In order to reduce the effect of correlations between data points from sequential configurations, we bin the data by groups of N_{bin} configurations. Because fits for this project were done in concert with other projects, $N_{\text{bin}} = 4$ was adopted. Comparisons of results using $N_{\text{bin}} = 2, 4$, and 6 on the ensembles used here show no significant change in the fit-result error bars or the bootstrap distributions. To account for correlations in the two-point correlator

TABLE III: Specific ensembles used in steps of the analyses. Setting priors is discussed in Sec. V A 1. Stability and goodness-of-fit tests done for $E(\mathbf{p})$ results are described in Sec. V A 2. κ -tuning and hyperfine-splitting results are given in Secs. VI A and VI B, respectively.

Lattice	setting priors	$E(\mathbf{p})$ tests, tuning κ , and the hyperfine splitting Δ_1
Fine	(0.0062, 0.031)	(0.0062, 0.031)
Coarse	(0.010, 0.050)	(0.007, 0.050)
Medium-coarse	(0.0194, 0.0484)	(0.0097, 0.0484)

data, the fitter uses the normalized, data-sample covariance matrix as an estimate of the correlation matrix. This matrix is remade for each bootstrap sample.

1. Priors, time ranges, N

We consider the setting of priors for the ground state parameters, excited-state amplitudes, and energy splittings separately. Ground-state ($\eta = 0$) parameters are well-determined by the data; thus, the ground-state priors can, and should, be negligibly constraining. In contrast, energy splittings and excited state amplitudes are not well determined by the data, and the related priors are chosen such that they put reasonable bounds on the parameters. The next paragraphs describe how the priors are set. Note that the same set of priors is used for all ensembles at a given lattice spacing, for all momenta in the range $|\mathbf{n}| = 0$ to 2, and for all κ and am'_q of a given meson type, e.g., charm pseudoscalars. The priors used are tabulated in Tables IV–VI.

We use information from a subset of our data, one ensemble per lattice spacing, to set the priors for the two-point-correlator fits. This is necessary because we do not have enough external knowledge to set them independently. The ensembles used to help set the priors are listed in Table III. Other ensembles are statistically independent of these ensembles and so the prior information can be viewed as external to fits on those ensembles. If possible, though, we do not want to exclude any data from our analysis, including the ensembles used in the setting of priors. For this reason, our procedure for setting priors keeps the amount of information we take from these ensembles to a minimum. Specifically, for a parameter P , we use averages over ranges of parameters, like the momentum, for the prior central value \tilde{P} and chose prior widths $\sigma_{\tilde{P}}$ that are broad enough to cover the expected results for an entire subset of fits; e.g., the same priors are used for fits with $|\mathbf{n}| = 0$ to 2.

To set ground-state priors, we first fit to large-time data with $N = 1$ in order to get a general idea of the ground-state parameter values. We then set $N > 1$ and fit correlators at low and high momenta to ascertain the range of values the ground state parameters may take. We set prior central values for the ground-state energy of the desired- and opposite-parity states, $aE_0(\mathbf{p})$ and $aE_0^p(\mathbf{p})$, at about the midpoint of the range seen in these fits.

To understand our logic for setting the prior widths for $aE_0(\mathbf{p})$ and $aE_0^p(\mathbf{p})$, recall that we use a Gaussian distribution for the prior \tilde{P} with a width $\sigma_{\tilde{P}}$. We set $\sigma_{a\tilde{E}_0}$ and $\sigma_{a\tilde{E}_0^p}$ large enough so that results across the entire momentum range used in the analysis should fall well within the $1-\sigma_{a\tilde{E}_0}$, or $1-\sigma_{a\tilde{E}_0^p}$, range of the distribution. After priors for the remaining parameters are set, we perform a complete set of fits and, for at least one ensemble at each lattice spacing, verify that, indeed, the final fit results for aE_0 and aE_0^p fit well within their respective prior distributions.

Priors for the ground-state amplitudes are loosely based on the preliminary $N > 1$ fits described above. In most cases, the central value is the nearest whole number to the average of these results. For the desired-parity state, the widths $\sigma_{\tilde{p}}$ are chosen such that they easily span the range of values seen in the fits. For the opposite parity states, which are substantially noisier, the widths span the distance between the prior central value and the observed range in the results by about $1-\sigma_{\tilde{p}}$.

Priors for all excited-state amplitudes were set to have a relatively small central value and a wide width. To set the prior for the energy splitting, we note that experimentally measured meson splittings are a few hundred MeV. We also bear in mind that the sum of a series of exponentials with a very small energy splitting is not a well-posed problem. Therefore, we chose the central value of the splitting to be several hundred MeV, slightly large, with a generous prior width. For example, on the fine lattice the prior for the splitting, $\ln(a\Delta E) = -1.45(1.0)$ is equivalent to $\Delta E \approx 550^{+950}_{-350}$ MeV.

In the charm sector, the opposite-parity partner of the $D_s(0^-)$, the $D_{s0}^*(0^+)$, is close to the DK threshold. In this case, the energy splitting should not be viewed as a meson mass splitting, and our choice of prior for the $D_{s0}^*(0^+)$ energy splitting may be inappropriate. The parity-partner signal is noisy, though, and in tests of the priors widths we see no change in the non-oscillating ground state energy $aE(\mathbf{p})$, which is our main interest. For details, see Sec. V A 2.

To choose the time ranges for the fits, (t_{\min}, t_{\max}) , we first look at the data to determine the time by which the error in the data, e.g. the relative error in the correlator, has increased substantially. This gives us a potential value for t_{\max} . From effective mass plots we can also see at what time slice the majority of the excited-state contamination has died off, giving us a potential value for t_{\min} . Constrained curve fitting is designed to reduce excited-state contamination of the lower-state fit parameters. Nevertheless, we do not see a significant reduction in the error from fitting to the smallest possible time slice, which requires including a larger number of states in the fit. For simplicity, we chose final time ranges that are the same for similar sets of data. These can be found in Table VII.

With the time range set, we do fits for increasing values of the number of (pairs of) states N and look for the ground-state energy to stabilize. We choose the final values of N to be the minimum value needed to be in the stable region; these are given in Table VII. Figure 1 shows representative plots of $aE(\mathbf{p})$ versus N from fits on the (0.0062, 0.031) fine ensemble. It is clear that for the minimum-value N , the central value of the fit result is always well within the stable region. In some cases, though, the (Hessian) error from the minimum- N fit is smaller than that in the stable region. One could remedy this by choosing to fit with more states. Unfortunately, an increase in the number of states leads to non-gaussian bootstrap distributions with a significant number of outliers — clearly non-physical fit results that contain ground states with low energies and very small amplitudes. Using the minimum possible number of states, no outliers have been seen in the distributions.

TABLE IV: Priors used for fine-ensemble two-point correlator fits for pseudoscalar and vector mesons. Priors for all higher amplitudes and splittings are the same as those for the first excited state. The fit-parameter numbers 15–20 label the second excited state and so on. A prior of $\ln(a\Delta E) = -1.45_{-1.0}^{+1.0}$ on the fine ensembles corresponds approximately to $\Delta E = 550_{-350}^{+950}$ MeV.

fit parameter	fit-parameter number	Charm Mesons		Bottom Mesons	
		pseudoscalar	vector	pseudoscalar	vector
E_0	1	0.90(40)	0.90(40)	1.75(60)	1.75(60)
E_0^P	2	1.0(40)	0.95(40)	1.85(60)	1.85(60)
$\ln(Z_{1S,0})$	3	1.0(2.0)	1.0(2.0)	1.0(3.0)	1.0(3.0)
$\ln(Z_{1S,0}^P)$	4	1.0(2.0)	1.0(2.0)	1.0(3.0)	1.0(3.0)
$\ln(Z_{d,0})$	5	-2.0(2.0)	-2.0(2.0)	-2.0(3.0)	-2.0(3.0)
$\ln(Z_{d,0}^P)$	6	-2.0(2.0)	-2.0(2.0)	-2.0(3.0)	-2.0(3.0)
$\ln(\Delta E)$	8	-1.45(1.0)	-1.45(1.0)	-1.45(1.0)	-1.45(1.0)
$\ln(\Delta E^P)$	9	-1.45(1.0)	-1.45(1.0)	-1.45(1.0)	-1.45(1.0)
$\ln(Z_{1S,1})$	10	-1.0(3.0)	-1.0(3.0)	-1.0(3.0)	-1.0(3.0)
$\ln(Z_{1S,1}^P)$	11	-1.0(3.0)	-1.0(3.0)	-1.0(3.0)	-1.0(3.0)
$\ln(Z_{d,1})$	12	-1.0(3.0)	-1.0(3.0)	-1.0(3.0)	-1.0(3.0)
$\ln(Z_{d,1}^P)$	13	-1.0(3.0)	-1.0(3.0)	-1.0(3.0)	-1.0(3.0)

TABLE V: Same as Table IV, but for the coarse ensembles. A prior of $\ln(a\Delta E) = -1.2_{-0.5}^{+0.5}$ on the coarse ensembles corresponds approximately to $\Delta E = 500_{-200}^{+300}$ MeV.

fit parameter	fit-parameter number	Charm Mesons		Bottom Mesons	
		pseudoscalar	vector	pseudoscalar	vector
E_0	1	1.10(40)	1.2(40)	2.00(40)	2.00(40)
E_0^P	2	1.30(40)	1.3(40)	2.10(40)	2.10(40)
$\ln(Z_{1S,0})$	3	1.0(2.0)	1.0(2.0)	1.0(2.0)	1.0(2.0)
$\ln(Z_{1S,0}^P)$	4	1.0(3.0)	0.1(3.0)	-1.0(2.0)	-0.1(2.0)
$\ln(Z_{d,0})$	5	-1.0(2.0)	-1.0(2.0)	-2.0(2.0)	-1.0(2.0)
$\ln(Z_{d,0}^P)$	6	-1.0(3.0)	-2.0(3.0)	-2.0(2.0)	-2.0(2.0)
$\ln(\Delta E)$	8	-1.2(0.5)	-1.2(0.5)	-1.2(0.5)	-1.2(0.5)
$\ln(\Delta E^P)$	9	-1.2(0.5)	-1.2(0.5)	-1.2(0.5)	-1.2(0.5)
$\ln(Z_{1S,1})$	10	-1.0(3.0)	-1.0(3.0)	-1.0(3.0)	-1.0(3.0)
$\ln(Z_{1S,1}^P)$	11	-1.0(3.0)	-1.0(3.0)	-1.0(3.0)	-1.0(3.0)
$\ln(Z_{d,1})$	12	-1.0(3.0)	-1.0(3.0)	-1.0(3.0)	-1.0(3.0)
$\ln(Z_{d,1}^P)$	13	-1.0(3.0)	-1.0(3.0)	-1.0(3.0)	-1.0(3.0)

TABLE VI: Same as Table IV, but for the medium coarse ensembles. A prior of $\ln(a\Delta E) = -1.0_{-0.5}^{+0.5}$ on the medium-coarse ensembles corresponds approximately to $\Delta E = 500_{-200}^{+300}$ MeV.

fit parameter	fit-parameter number	Charm Mesons		Bottom Mesons	
		pseudoscalar	vector	pseudoscalar	vector
E_0	1	1.38(50)	1.46(50)	2.35(40)	2.38(50)
E_0^P	2	1.50(60)	1.58(60)	2.48(50)	2.50(50)
$\ln(Z_{1S,0})$	3	0.48(1.0)	0.95(1.0)	0.12(1.4)	0.60(1.0)
$\ln(Z_{1S,0}^P)$	4	-0.65(1.0)	0.20(1.0)	-1.0(2.0)	0.1(2.0)
$\ln(Z_{d,0})$	5	-0.90(1.0)	-0.74(1.0)	-1.15(1.0)	-0.8(1.0)
$\ln(Z_{d,0}^P)$	6	-2.4(1.4)	-1.8(2.0)	-2.5(3.0)	-1.8(3.0)
$\ln(\Delta E)$	8	-1.0(0.5)	-1.0(0.5)	-1.0(0.5)	-1.0(0.5)
$\ln(\Delta E^P)$	9	-1.0(0.5)	-1.0(0.5)	-1.0(0.5)	-1.0(0.5)
$\ln(Z_{1S,1})$	10	-1.0(3.0)	-1.0(3.0)	-1.0(3.0)	-1.0(3.0)
$\ln(Z_{1S,1}^P)$	11	-1.0(3.0)	-1.0(3.0)	-1.0(3.0)	-1.0(3.0)
$\ln(Z_{d,1})$	12	-1.0(3.0)	-1.0(3.0)	-1.0(3.0)	-1.0(3.0)
$\ln(Z_{d,1}^P)$	13	-1.0(3.0)	-1.0(3.0)	-1.0(3.0)	-1.0(3.0)

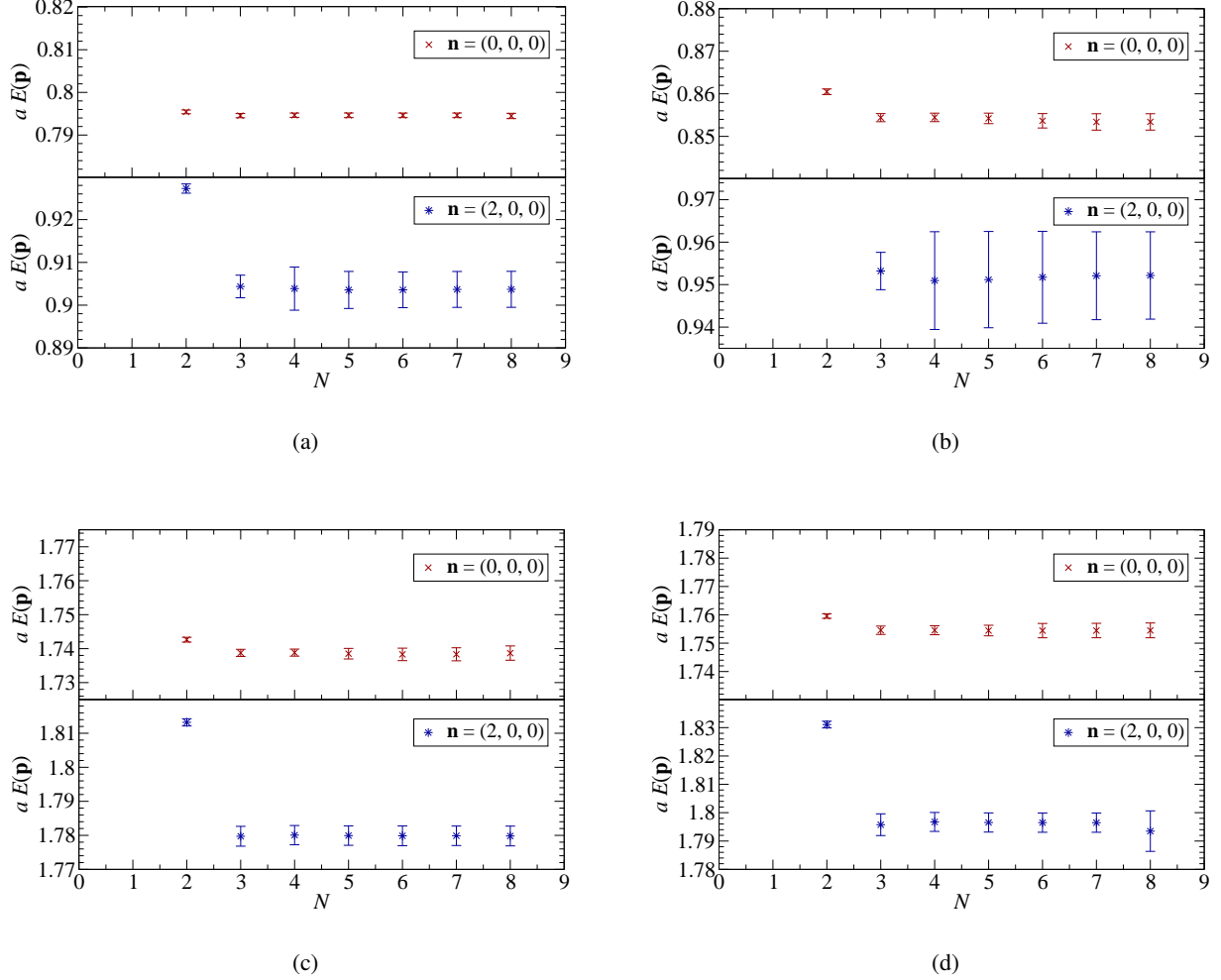


FIG. 1: Fitted values of $aE(\mathbf{p})$ vs. the number of (pairs of) states N for $\kappa = 0.127$, charm-type (a) pseudoscalar and (b) vector mesons and $\kappa = 0.090$, bottom-type (c) pseudoscalar and (d) vector mesons on the (0.0062, 0.031) fine ensemble. Results shown are for mesons with momenta $\mathbf{n} = (0, 0, 0)$ and $(2, 0, 0)$. Errors are Hessian.

2. Tests of Stability and Goodness-of-fit

Having set the priors, time range, and number of states for the fits, we check the stability of the results and goodness of fit in several ways. For result stability, we check the effects of the time range used, the number of (pairs of) states N , and changes to the prior widths; we also compare the priors to the fit results. We look at a representative subset of fits for each lattice spacing: pseudoscalar and vector meson correlators at two different κ values (one for charm and one for bottom) for a given light-valence mass, on one ensemble per lattice spacing, and with momenta $\mathbf{n} = (0, 0, 0)$ and $(1, 1, 1)$ or $(2, 0, 0)$. The specific values of κ , am'_q , and (am'_l, am'_s) vary from test to test, and in some cases tests are extended to other values. A description of the data used in the tests discussed here can be found in Table VIII.

TABLE VII: Time range $t_{\min}-t_{\max}$ and number of (pairs of) states N used in two-point correlator fits at each lattice spacing. For the time range, the first (second) number in parenthesis is t_{\min} for the 1S-smearred (local) correlator; t_{\max} is the same for both correlators.

Lattice spacing	Time range	N
Fine	(2, 4)–25	3
Coarse	(2, 8)–15	2
Medium-coarse	(5, 6)–15	2

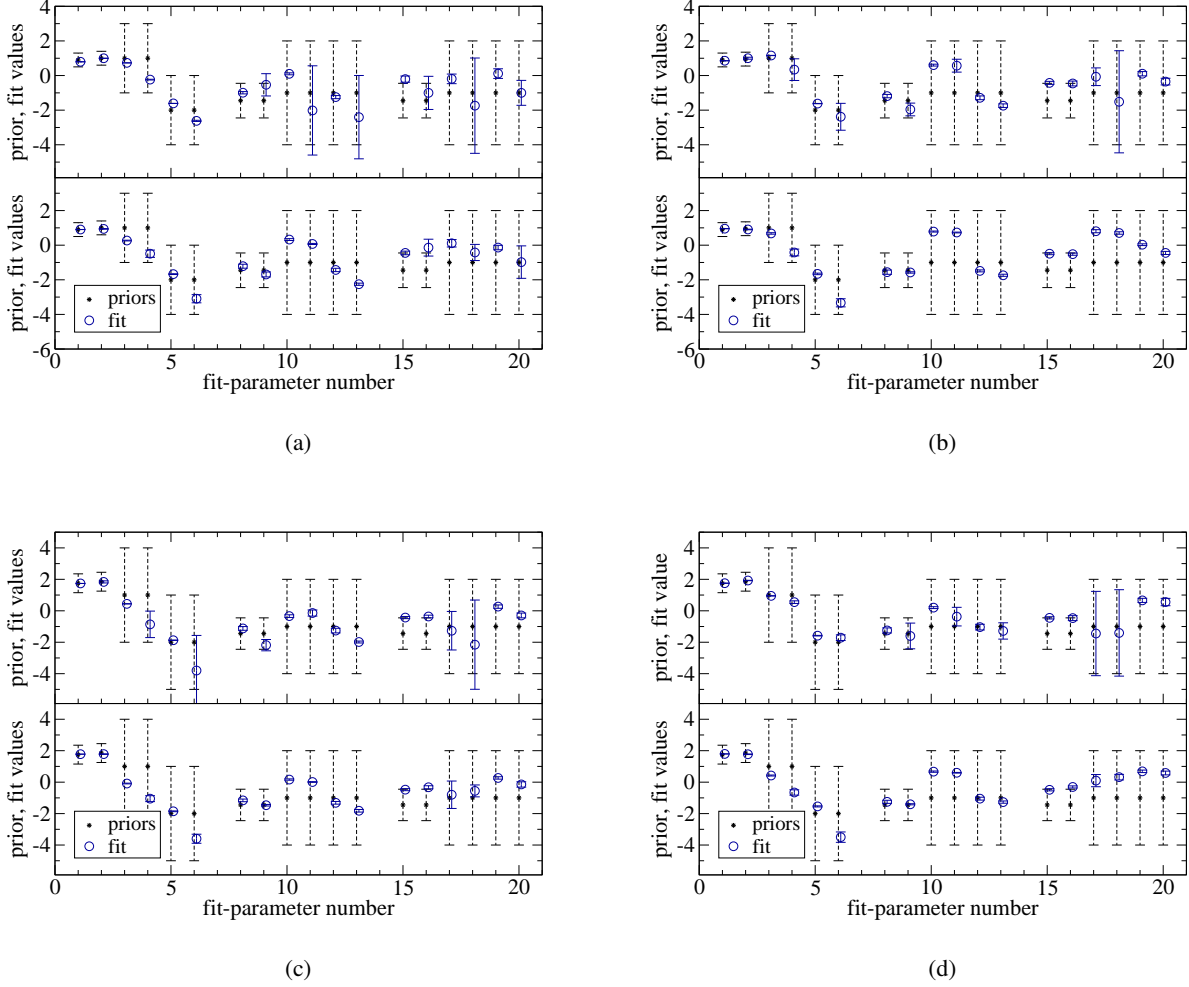


FIG. 2: Fit results shown as open (blue) circles are overlaid on the priors, black dots with dashed widths, for charm-type (a) pseudoscalar and (b) vector mesons and bottom-type (c) pseudoscalar and (d) vector mesons on the (0.0062, 0.031) fine ensemble. $\kappa = 0.127$ and 0.090 for charm- and bottom-type mesons, respectively; $am'_q = 0.0272$. The upper [lower] plot is from a fit where the meson has momentum of $\mathbf{n} = (0, 0, 0)$ [(2, 0, 0)]. The fit-parameter numbers are defined in Table IV. In each panel, the leftmost cluster corresponds to quantities from the ground state; the middle cluster corresponds to the first excited state; and the right most cluster to the second excited state. Errors on the fit results are Hessian. For clarity, fit results are offset along the x -axis.

For the time-range tests, we vary t_{\min} over two to four time slices, increasing N if appropriate, and vary t_{\max} over five to ten time slices. We verify that there are no changes in the fit results beyond expected fluctuations.² For number-of-states tests, we

TABLE VIII: Data used in stability and goodness-of-fit tests.

Lattice	ensemble	κ	am'_q
Fine	(0.0062, 0.031)	0.127; 0.090 or 0.093	0.0272
Coarse	(0.007, 0.050)	0.122; 0.086	0.0415
Medium-coarse	(0.0097, 0.0484)	0.125; 0.070	0.0484

² In one case, $\kappa = 0.086$, coarse (0.010, 0.005), although the ground-state energy is stable as t_{\max} is varied, the value of χ^2/dof becomes large as t_{\max} is increased beyond the final value ($t_{\max} = 15$). This ensemble is not used directly for κ tuning or hyperfine splitting determinations as explained in the

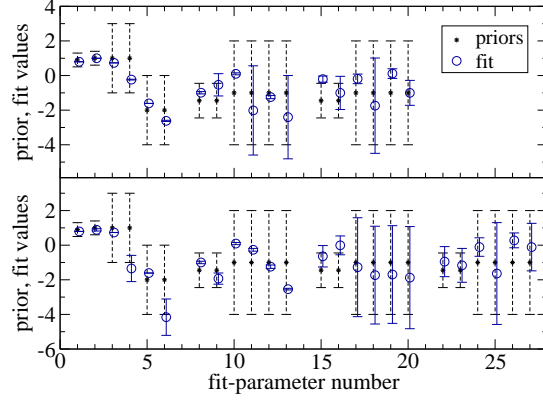


FIG. 3: Fit results shown as open (blue) circles are overlaid on the priors, black dots with dashed widths, for charm-type mesons on the (0.0062, 0.031) fine ensemble. $\kappa = 0.127$; $am'_q = 0.0272$; $\mathbf{n} = (0, 0, 0)$. The upper plot is the same as the upper left (pseudoscalar) panel of Fig. 2 (a). The lower plot is from a fit which only differs by the use of $N = 4$ pairs of states. The fit-parameter numbers are defined in Table IV. In each panel, the leftmost cluster corresponds to quantities from the ground state; the middle cluster corresponds to the first excited state; the next cluster corresponds to the second excited state and so on. The (desired-parity) ground-state quantities are stable to this change while other, excited-state, parameters are not. Errors on the fit results are Hessian. For clarity, fit results are offset along the x -axis.

verify that the result is stable as N is increased. Figure 1 shows example results for the (0.0062, 0.031) fine ensemble. Similar results are seen for the coarse and medium-coarse ensembles and for the ground-state amplitudes Z_{1S} and Z_d .

For prior-width tests, we reduce the widths by a factor of two for the non-oscillating ground state quantities and the energy splittings and repeat the fits. All changes observed are within statistical errors and, in most cases, the changes are substantially smaller than one σ . For charm, we also test for effects of the DK threshold near the $D_{s0}^*(0^+)$ state. This splitting is 50 to 100 MeV, which is a several- $\sigma_{\Delta_{aE_p}}$ deviation from our prior central value. We ran separate tests on each lattice spacing using a prior width of $\sigma_{\Delta_{aE_p}} = 2.5$ for the oscillating-state energy splitting. In units of MeV, this puts a 50-MeV splitting within $1\sigma_{\Delta_{aE_p}}$ of the prior central value. The ground and first-excited-state energies of the oscillating state are affected by this change but not in a systematic way. This indicates that the oscillating-state signal is not strong in our data. Our main interest, though, is the non-oscillating ground state energy $aE(\mathbf{p})$; this value is unaffected by the change in $\sigma_{\Delta_{aE_p}}$.

In addition, we compare fit results with their priors. Figure 2 gives examples of these comparisons for fits on the (0.0062, 0.031) fine ensemble for charm- and bottom-type mesons. The x -axis labels the fit-parameter number, defined in Table IV; the ground-state energy and amplitudes of the desired-parity state are at positions 1, 3, and 5. We find that fit results for ground-state quantities are well within the prior widths. For excited states, in some cases the fitter simply returns the prior value, indicating that the quantity is not constrained by the data. In other cases, the results appear to be constrained by the data, indicating that some excited-state signal is in the correlator and the fitter adjusts the amplitudes to absorb it. Although it may appear in Fig. 2 that a number of excited-state quantities are well-determined, this is an artifact of a minimum- N fit; unlike the ground-state parameters, the excited state results are not stable as N is increased. For example, Fig. 3 compares the fit results shown in the upper left (pseudoscalar) panel of Fig. 2 (a), which uses $N = 3$, with a fit which only differs by the use of $N = 4$. The comparison demonstrates that the (desired-parity) ground-state quantities are stable to the change in N while other, excited-state, parameters are not.

For goodness-of-fit we begin by looking at the augmented χ^2/dof for each fit and verify that it is ≈ 1 or smaller, where “ ≈ 1 ” is based on the 80% range of the χ^2/dof distribution for a given number of degrees of freedom. As a final check, we overlay the result on an effective-mass plot. We define the “effective energy”

$$2aE_{\text{eff}}(\mathbf{p}) = \ln [C(t)/C(t + 2a)] \quad (5.1)$$

using a step of two time units in order to accommodate the oscillating contribution from the opposite-parity state. Figure 4 shows plots comparing $aE_{\text{eff}}(\mathbf{p})$ to the fit result on the (0.0062, 0.031) fine ensemble. The ground-state-energy result from the

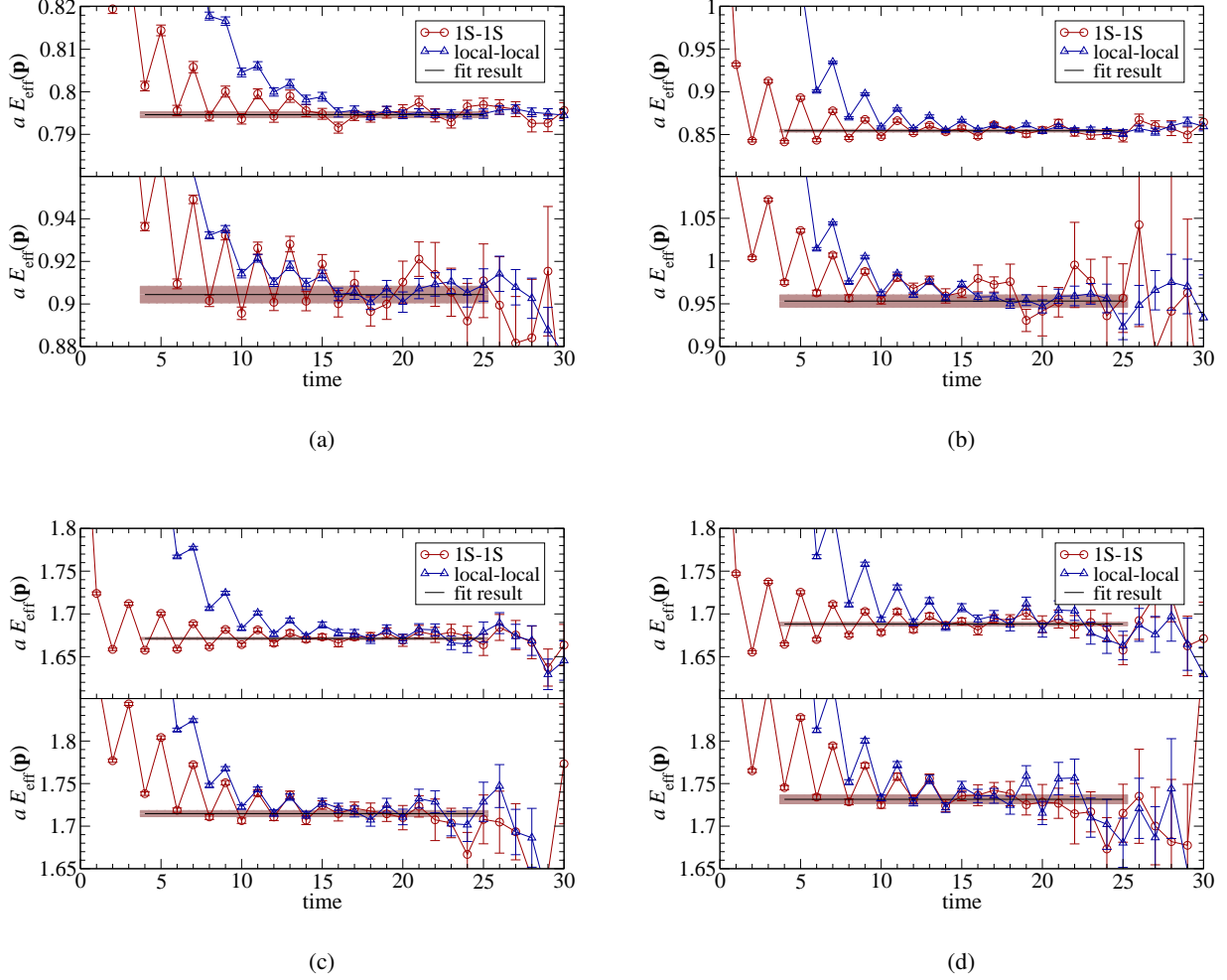


FIG. 4: Effective energy plots, $aE_{\text{eff}}(\mathbf{p})$, for charm-type (a) pseudoscalar and (b) vector mesons and bottom-type (c) pseudoscalar and (d) vector mesons on the (0.0062, 0.031) fine ensemble. $\kappa = 0.127$ and 0.093 for charm- and bottom-type mesons, respectively; $am_q = 0.0272$. The upper [lower] plot is from a fit where the meson has momentum of $\mathbf{n} = (0, 0, 0)$ [$\mathbf{n} = (2, 0, 0)$]. Open (blue) triangles mark the local correlator and open (red) circles mark the 1S-smear correlator. Lines connecting the data points are simply to guide the eye; they are not a fit. The unadorned black line is the multi-correlator fit result and the shaded band marks the average 68% bootstrap error.

multiple-state fit is shown as a straight line segment over the time range fit. The band encompasses the average 68% bootstrap error. In each case, the fit result nicely matches the effective-energy plateau.

B. The kinetic mass M_2

Given results for $aE(\mathbf{p})$, we fit data where $|\mathbf{n}| \leq \sqrt{3}$ to Eq. (4.6) to determine the pseudoscalar and vector kinetic meson masses. Fits use a correlation matrix constructed from the bootstrap distributions. The tables in Appendix B give results for aM_2 , aM_2^* , and $a\bar{M}_2$ on the ensembles used for tuning, listed in Table III. Included in the tables are the χ^2/dof and the probability that χ^2 would exceed the value from the fit, known as the p value [45]. Typical dispersion relation fits are shown for the (0.0062, 0.031) fine ensemble in Fig. 5.

In addition to statistical errors, we consider uncertainties from unphysical sea-quark masses, mistuning of the valence strange quark, and discretization. The noise in \bar{M}_2 makes it difficult to discern how \bar{M}_2 depends on the sea-quark masses. The \bar{M}_1 data is much cleaner, though, and we can use it to estimate the sea-quark error on \bar{M}_2 , and hence κ . To do this, we first note that, cf. Eq. (2.12),

$$aM_1 = am_1 + a\bar{\Lambda}_{\text{lat}} + O(1/m_Q) \quad (5.2)$$

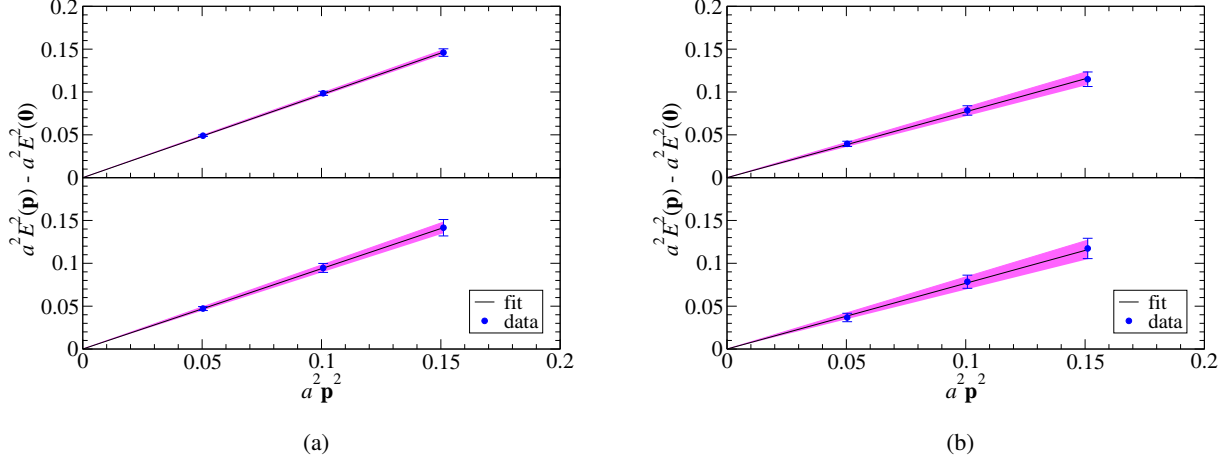


FIG. 5: Results of fits to the dispersion relation for (a) charm-type ($\kappa = 0.127$) and (b) bottom-type ($\kappa = 0.0923$) mesons on the (0.0062, 0.031) fine ensemble. (Blue) dots are the data. A black line shows the fit result with the (pink) shaded band showing the one-sigma error from the fit. Upper panels show results for pseudoscalars and lower for vectors.

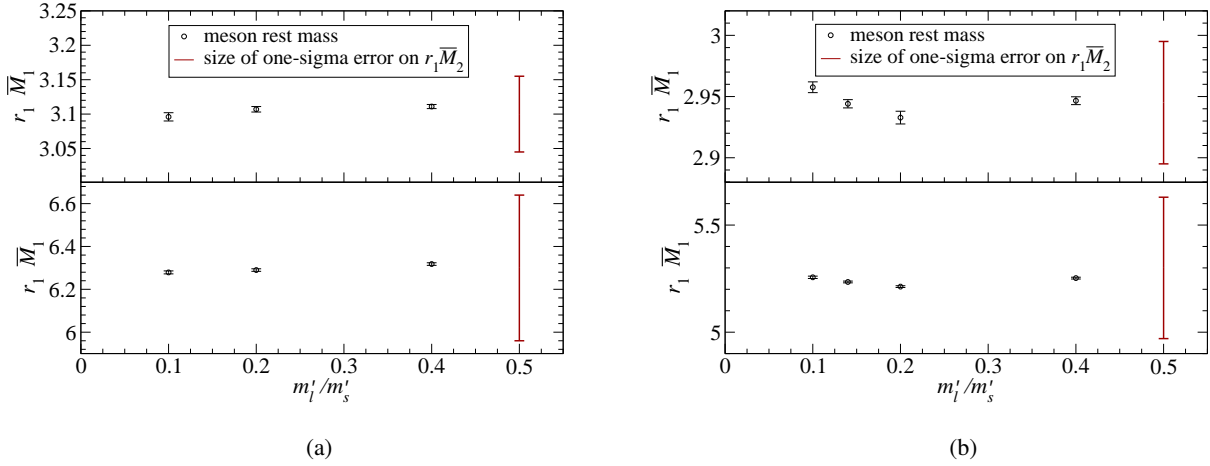


FIG. 6: The spin-averaged meson rest mass in physical units versus the ratio of the light to strange sea-quark masses m'_l/m'_s for the (a) fine and (b) coarse ensembles. Error bars are statistical only, from the average 68% bootstrap error. On the far right of the plot is a (red) bar indicating the size of the one-sigma statistical error on $r_1 \bar{M}_2$. The upper-panel plot is for charm-type mesons, lower is for bottom-type. Values of κ used are 0.127, 0.0923 on the fine ensembles with $am'_q = 0.0272$ and κ 0.122, 0.086 on the coarse ensembles with $am'_q = 0.0415$.

$$aM_2 = am_2 + a\bar{\Lambda}_{\text{lat}} + O(1/m_Q) \quad (5.3)$$

where am_1 and am_2 capture the leading heavy-quark dependence and $\bar{\Lambda}_{\text{lat}}$ depends only on the light degrees of freedom. Taking $a\bar{\Lambda}_{\text{lat}}$ to be the same for both $a\bar{M}_1$ and $a\bar{M}_2$ (see Appendix A and Ref. [46]) we can estimate the size of the effect of non-physical (light) sea quark masses on $a\bar{\Lambda}_{\text{lat}}$, and hence aM_2 , by studying the behavior of aM_1 as the light sea-quark masses are varied.

In Fig. 6, we plot the spin-averaged meson rest mass $r_1 \bar{M}_1$ versus the ratio of the light to strange sea-quark masses m'_l/m'_s for the coarse and fine ensembles used here. On the far right of each plot is a bar indicating the size of the 1- σ statistical error on $r_1 \bar{M}_2$; for fine this is from the (0.0062, 0.031) ensemble and for coarse the (0.007, 0.050) ensemble. The light sea-quark mass dependence is negligible compared to the statistical error on $r_1 \bar{M}_2$. We find similar behavior for the medium-coarse ensemble.

We must also consider how the non-physical value of the strange sea-quark mass affects \bar{M}_2 . The strange sea-quark mass is mistuned by an amount $0.19am'_s$, $0.31am'_s$ and $0.12am'_s$ on the fine, coarse, and medium-coarse ensembles, respectively. The continuum chiral perturbation theory expression for the heavy-light spin-averaged mass [47] shows that the leading sea-quark

dependence of \overline{M}_2 is proportional to the sum over the sea-quark masses, $2m'_l + m'_s$. Hence, varying am'_l tells us about the effect of varying am'_s . Figure 6 shows that a change of $0.3am'_s$ in am'_l has a negligible effect on \overline{M}_2 , so we conclude that the mistuning of am'_s has a negligible effect as well.

The tuned value of the strange-quark mass on each ensemble is given in Table I. On the fine lattice, the valence-quark mass used in the simulation, $am'_q = 0.0272$, differs from the physical value $am_s = 0.0252$ by 0.0020. A comparison of our results for $a\overline{M}_2$ in Table XVIII shows that even a deviation in am'_q of twice this size does not discernibly affect $a\overline{M}_2$. The situation is similar for the coarse and medium-coarse results. For the coarse ensembles, the simulation mass $am'_q = 0.03$ differs by 0.0044 from the tuned value of am_s . Table XIX shows that $a\overline{M}_2$ is barely affected at the $1-\sigma_{a\overline{M}_2}$ level as am'_q changes by over twice this size. For the medium-coarse ensembles, the simulation mass of 0.0484 differs from the tuned strange-quark mass by 0.0058. A comparison of the values of $a\overline{M}_2$ in Table XX shows that a deviation in am'_q just under twice this size yields, at most, a $1-\sigma_{a\overline{M}_2}$ variation in $a\overline{M}_2$. Therefore, we take our results of $a\overline{M}_2$ at $am'_q = 0.0272$, 0.03, and 0.0484 as the masses of the B_s and D_s on the fine, coarse and medium-coarse ensembles, respectively, with no additional error for valence-mass mistuning.

In Appendix A, we derive an expression for the discretization error in M_2 , $M_2 = M_{\text{continuum}} + \delta M_2$. The result, Eq. (A22), can be written

$$\delta M_2 = \frac{\overline{\Lambda}^2}{6m_2} \left[5 \left(\frac{m_2^3}{m_4^3} - 1 \right) + 4w_4(m_2a)^3 \right], \quad (5.4)$$

replacing $\langle p^2 \rangle$ of Eq. (A22) with $\overline{\Lambda}^2$. Expressions for the short-distance coefficients m_2 , m_4 , and w_4 are given in Appendix A [14, 23]. To estimate the discretization error, we use values of the physical (pole) quark mass (1.4 GeV for charm and 4.2 GeV for bottom) for m_2 in the prefactor of Eq. (5.4), and $\overline{\Lambda} = 0.7$ GeV. Using these values, u_0 from Table II, and κ_{crit} from Table XVII yields the values of δM_2 shown in Table IX. The error estimate in Eq. (5.4) pertains to the kinetic mass, but the main focus here is the tuning of κ . After tuning, we shall propagate this error from M_2 to κ_c and κ_b .

C. Fitting Summary

The preceding subsections contain many details intended for those engaged in similar analyses. In this section, we re-emphasize the main features of the analysis. Because, in this and related [3–8] work, we are interested in the ground state, we do not dwell on the excited states here.

Our priors are guided by the data, using one ensemble to set them and (generally) other ensembles for physical results. We choose a time range such that the fit results for the ground state are stable, listed in Table VII. We also test for stability as the number N of (pairs of) exponentials grows—as shown in one example in Fig. 1—and choose the minimum value of N for which the central value is stable within errors. The errors on the ground-state amplitudes and energies are always determined by the data, not the priors, as shown in Fig. 2 and 3. (In many cases, even excited-state information is data-determined, not prior-determined.) Figure 4 shows that the fits agree with the effective energies. (Note that the oscillations of aE_{eff} at small t are to be expected with staggered quarks.) In conclusion, the constrained curve fitting for $E(\mathbf{p})$ has worked as advertised, subsuming the subjectivity of fit ranges and different choices of N into robust results for both central value and error bar. Figures 5 and 6 show that, once $E(\mathbf{p})$ is well-determined, we can straightforwardly obtain the kinetic mass M_2 and the hyperfine splitting.

VI. RESULTS

In this section, we present the main results of these calculations, including our error analysis. Section VIA focuses on the tuned values of κ_c and κ_b , Sec. VIB on the D_s and B_s hyperfine splittings, and Sec. VIC on the critical value of the hopping

TABLE IX: The relative error in the tuned hopping parameter $\delta\kappa/\kappa$ due to discretization effects in the kinetic meson mass. The ensembles used are (0.0062, 0.031), (0.007, 0.050), and (0.0097, 0.0484) for the fine, coarse, and medium-coarse lattices, respectively. Values of κ are 0.127 and 0.0923 on fine; 0.122 and 0.086 on coarse; and, 0.122 and 0.076 on medium-coarse. The $[\dots]$ denotes the quantity in brackets in Eq. (5.4). We use $(\overline{\Lambda}^2/6m_{\text{ch}}) = 0.0583$ and $(\overline{\Lambda}^2/6m_{\text{bot}}) = 0.0194$ to convert the $[\dots]$ to δM_2 . Values of $\delta\kappa/\kappa$ are given as fractions not a percentage.

lattice spacing	charm					bottom				
	m_0a	$[\dots]$	δM_2	$\frac{dm_2a}{dm_0a}$	$\frac{\delta\kappa}{\kappa}$	m_0a	$[\dots]$	δM_2	$\frac{dm_2a}{dm_0a}$	$\frac{\delta\kappa}{\kappa}$
fine	0.391	1.31	0.0763	0.843	-0.0086	2.08	16.8	0.327	0.880	-0.0256
coarse	0.565	2.37	0.1384	0.831	-0.0203	2.62	23.6	0.459	0.899	-0.0440
medium-coarse	0.682	3.18	0.1857	0.830	-0.0346	3.56	37.2	0.724	0.922	-0.0756

parameter κ_{crit} .

A. The tuning of κ_c and κ_b

As discussed in Sec. VB, effects from non-physical sea-quark masses and the mistuning of the valence strange-quark mass are negligible compared to the statistical error on $a\overline{M}_2$. In that section, we explain why taking $a\overline{M}_2$ at certain values of am'_q is an acceptable approximation to $a\overline{M}_2$ at the tuned physical strange-quark mass. We choose to tune κ at those same am'_q , which are $am'_q = 0.0272$ on the (0.0062, 0.031) fine ensemble, $am'_q = 0.03$ on the (0.007, 0.050) coarse ensemble, and $am'_q = 0.0484$ on the (0.0097, 0.0484) medium-coarse ensemble.

To obtain the tuned κ for the charm (bottom) quark, κ_c (κ_b), we want to interpolate \overline{M}_2 to the PDG value of the spin-averaged D_s (B_s) mass [45]. In practice, it is simpler to do the interpolation with the meson mass in lattice units. Hence, we linearly interpolate $a\overline{M}_2$ to $a\overline{M}_{\text{PDG}}$, the PDG value for the meson mass converted to lattice units with a from Table I. This interpolation is repeated for the entire bootstrap distribution of $a\overline{M}_2$. We then estimate the statistical error on κ as the average 68% bootstrap error described in Sec. IV A. The discretization error in M_2 , δM_2 , is given by Eq. (5.4), and is always positive. This results in a single-sided, negative error bar on κ . We convert δM_2 to the error, $\delta\kappa$, using $dM_2/d\kappa \approx dm_2/d\kappa$ and expressions for m_0a and m_2a given in Appendix A. The $\delta\kappa$ are given in Table IX. The experimental errors on the PDG values are negligible. The remaining errors to consider are those which appear in the conversion between lattice and physical units. The error in the determination of r_1/a is negligible, so we only need to consider the error in r_1 , given in Eq. (3.2).

The error on r_1 is propagated to an error on a^{-1} and then to an error on $a\overline{M}_{\text{PDG}}$, denoted σ_{PDG} . Table X gives the values of the PDG meson masses used in this work and tabulates their spin-averaged mass and hyperfine splitting. Table XI gives the spin-averaged mass in lattice units. The uncertainty σ_{PDG} is propagated to κ using the standard error formula $\sigma_\kappa = \sigma_{\text{PDG}}/s$, where s is the slope used in the interpolation. Table XII gives the error budget for κ_c and κ_b , and Table XIII lists the final tuned results.

TABLE X: PDG values of the pseudoscalar and vector masses for the D_s and B_s mesons and the hyperfine splitting Δ [45]. Also listed is the derived quantity \overline{M} , the spin-averaged mass.

	M (GeV)	M^* (GeV)	\overline{M} (GeV)	Δ (MeV)
D_s	1.96849(34)	2.1123(5)	2.0763(4)	143.9(4)
B_s	5.3661(6)	5.4120(12)	5.4005(9)	46.1(1.5)

TABLE XI: Spin-averaged PDG masses converted to lattice units with an error from the uncertainty in the lattice spacing a . Values of a used in the conversion can be found in Table I.

Ensemble	$a\overline{M}_{D_s}$	$a\overline{M}_{B_s}$
Fine (0.0062, 0.031)	$0.884^{+0.009}_{-0.023}$	$2.299^{+0.023}_{-0.060}$
Coarse (0.007, 0.050)	$1.242^{+0.012}_{-0.032}$	$3.230^{+0.031}_{-0.083}$
Medium-coarse (0.0097, 0.0484)	$1.529^{+0.015}_{-0.039}$	$3.977^{+0.038}_{-0.102}$

TABLE XII: Percent errors in the tuned κ and the total error. For several sources of uncertainty, we determined that the error was smaller than the precision of these calculations. This is indicated by an entry of “0.0” in the table.

Uncertainty	Charm			Bottom		
	Fine	Coarse	Medium-coarse	Fine	Coarse	Medium-coarse
Statistical	1.26	0.57	0.53	5.0	9.1	5.6
Discretization	(0, -0.86)	(0, -2.0)	(0, -3.46)	(0, -2.6)	(0, -4.4)	(0, -7.56)
Sea-quark masses	0.0	0.0	0.0	0.0	0.0	0.0
am_s mistuning	0.0	0.0	0.0	0.0	0.0	0.0
Unit conversion (a)	(+0.90, -0.35)	(+0.49, -0.19)	(+0.77, -0.30)	(+1.7, -0.64)	(+1.9, -0.72)	(+1.76, -0.66)
Total	(1.5, 1.6)	(+0.75, -2.1)	(+0.93, -3.5)	(+5.3, -5.7)	(+9.3, -10.1)	(+5.9, -9.4)

B. The rest mass and hyperfine splitting

In this section, we discuss the uncertainties in our calculation of the hyperfine splitting and compare our final results, for the B_s and D_s systems, with the PDG values. To support the discussion, we tabulate our results for the pseudoscalar and vector meson rest masses and the hyperfine splitting, $aM, aM^*, a\Delta_1, r_1\Delta_1$, in Tables XXI–XXIII in Appendix C. Statistical errors in these tables are the average 68% bootstrap errors described in Sec. IV A. The other errors we consider are the mistuning of the valence strange-quark mass, unphysical sea-quark masses, the uncertainty in the tuning of κ , discretization effects, and the conversion to physical units. For the central value, at each lattice spacing, we take $a\Delta_1$ at the tuned values of κ_c and κ_b , linearly interpolating in κ when necessary.

PDG results for the hyperfine splitting show a weak dependence on the light-quark valence mass, so we expect the mistuning in the simulated valence strange-quark mass to have a negligible effect.³ The simulation valence masses $am'_q = 0.0272, 0.03, 0.0484$ for the fine, coarse, and medium-coarse lattices, respectively, differ from the physical am_s given in Table I by 0.0020, 0.0044, 0.0058, respectively. Tables XXI–XXIII show that, indeed, these small mistunings have a negligible effect on the hyperfine splitting. Hence, we do not interpolate to am_s ; rather, we take $a\Delta_1$ at the valence masses am'_q listed above as the result at the physical strange valence-quark mass and take the error for this approximation to be negligible.

To estimate the error due to the non-physical values of the sea-quark masses we use partially-quenched chiral perturbation theory. The needed expression is derived in Appendix D and we repeat Eq. (D1) here for convenience. The hyperfine splitting $M_x^* - M_x$ of a heavy-light meson with light-valence quark x is

$$M_x^* - M_x = \Delta - \frac{\Delta g_\pi^2}{8\pi^2 f^2} \delta_{\log} + 2\Delta^{(\sigma)}(2m_l + m_s) + 2\Delta^{(a)}m_x, \quad (6.1)$$

where δ_{\log} contains the chiral logs, m_l and m_s are the light and strange sea-quark masses, and $\Delta^{(\sigma)}$ and $\Delta^{(a)}$ are counter terms which must be determined from the lattice data. Working at a fixed value of m_x , we can use the difference of splittings at different values of m_l to determine $\Delta^{(\sigma)}$. Given $\Delta^{(\sigma)}$, we can find the difference between the splitting at simulation values of (m'_l, m'_s) and the physical values $(m_{l,\text{phys}}, m_{s,\text{phys}})$. We take this difference as the error due to the non-physical sea-quark masses.

We have tabulated values of the hyperfine splitting in physical units, $r_1\Delta_1$, in Appendix C 2. Figure 7 shows how $r_1\Delta_1$ varies with the light sea-quark mass on fine and coarse lattices. From Fig. 7, it is clear that, due to statistical variation in the splitting, using the difference in the central values of splittings from any two points will yield different values for $\Delta^{(\sigma)}$. For the fine and coarse ensembles, we look only at the $am_l/am_s = 0.4$ to 0.1 and $am_l/am_s = 0.4$ to 0.2 differences and take the one that gives the larger error; for medium coarse, we have no $am_l/am_s = 0.1$ data and so take the error from the $am_l/am_s = 0.4$ to 0.2 difference.

For the error estimate, we take $f = 131$ MeV and $g_\pi = 0.51$ [48]. We relate meson to quark masses by

$$M_{xy}^2 = B_0(m_x + m_y) \quad (6.2)$$

where B_0 is determined empirically with $r_1B_0 = 6.38, 6.23, 6.43$ on the fine, coarse, and medium-coarse lattices, respectively. These values of B_0 come from tree-level fits to MILC light-meson data, as described in Refs. [2, 11, 35]. We calculate $\Delta^{(\sigma)}$ for each meson type, B_s and D_s , at each lattice spacing. We then calculate the difference

$$(M_x^* - M_x)_{\text{sim}} - (M_x^* - M_x)_{\text{phys}} \quad (6.3)$$

where the subscript “sim” (“phys”) denotes simulation (physical) sea-quark mass inputs (am_l, am_s) . For the physical masses, we use $(am_{l,\text{phys}}, am_{s,\text{phys}}) = (0.00092, 0.0252), (0.00125, 0.0344), (0.00154, 0.0426)$ for the fine, coarse, and medium-coarse lattices, respectively. These values of the quark masses are taken from Ref. [11], after adjustment for the r_1 scale used here.

TABLE XIII: Final tuned results for κ_c and κ_b with the total error.

	Fine	Coarse	Medium-coarse
κ_c	0.127(2)	0.1219 ⁺⁹ ₋₂₅	0.122 ⁺¹ ₋₄
κ_b	0.090(5)	0.082(8)	0.077 ⁺⁵ ₋₇

³ For $X = B$ or D , the difference between the $M_{X_s^*} - M_{X_s}$ splitting and the $M_{X^*} - M_X$ splitting is measured to be about 1% or less [45].

The simulation masses are those on the the (0.0062, 0.031) fine, (0.007, 0.050) coarse, and (0.097, 0.0484) medium-coarse ensembles. The error calculated in this manner is labeled “sea-quark masses” in Tables XIV and XV.

For the uncertainty in $a\Delta_1$ due to the error in κ , recall that the non-negligible sources of error in κ , from Table XII in Sec. VI A, are statistics, units conversion, and discretization error in M_2 . Because we want to consider discretization errors separately from all others, we start by considering only the κ -tuning error that comes from statistics and units-conversion. To convert the error in κ to an error in $a\Delta_1$, we look at the change in $a\Delta_1$ between two values of κ on the (0.0062, 0.031) fine, (0.007, 0.050) coarse, and (0.0097, 0.0484) medium-coarse ensembles; specific values can be found in Tables XXI–XXIII. This is the error labeled “ κ tuning” in Tables XIV and XV.

For the D_s (B_s) meson, Table XIV (XV) gives the error budget for $a\Delta_1$ at each lattice spacing, from all sources *except* discretization. These are statistics, valence-mass mistuning, unphysical sea-quark masses, and κ tuning. In Fig. 8, these values are plotted as black, filled dots.

We now consider the three, distinct sources of discretization error in $a\Delta_1$. The first is indirect, coming from the discretization error in aM_2 , which is propagated to an error on κ as discussed in Sec. VI A. This error can be traced to a mismatch between the spin-independent $O(\mathbf{p}^4)$ terms in Eq. (2.8) (not given explicitly) and the corresponding terms in the effective Lagrangian for continuum QCD. These terms contribute to $a\bar{M}_2$ as discussed in Appendix A. The second source of discretization error is a direct result of the lattice-continuum mismatch of the dimension-seven operator $\{i\boldsymbol{\sigma} \cdot \mathbf{B}, \mathbf{D}^2\}$ [23].⁴ The third source of discretization error is the $O(\alpha_s)$ mismatch in the coefficient of the $i\boldsymbol{\sigma} \cdot \mathbf{B}$ operator in Eq. (2.10). For the discussion of error estimates below, it is useful to recall that the heavy-quark dynamics associate m_2 with the physical quark mass. Mismatches between m_2 and the generalized masses associated with other operators capture the heavy-quark discretization effects. We now give numerical estimates of the error from each source.

Our estimate of discretization error in $a\bar{M}_2$ and its inclusion in the error on κ is discussed in Sec. VI A. In Fig. 8, the value of $r_1\Delta_1$ with an error that includes *only* the uncertainty due to the discretization error on κ is shown as an open (blue) circle with a dashed error bar. Note, as described in Sec. V B, this uncertainty estimate depends on one’s choice of Λ_{QCD} . In this paper, we use $\Lambda_{\text{QCD}} = 0.7$ GeV. Choosing $\Lambda_{\text{QCD}} = 0.5$ GeV would cut the error on κ in half and decrease the error on $r_1\Delta_1$.

Next we estimate the contribution from the dimension-seven operator $\{i\boldsymbol{\sigma} \cdot \mathbf{B}, \mathbf{D}^2\}$. Using the notation of Ref. [23], summarized in Sec. A 4, this operator’s contribution to the hyperfine splitting has a coefficient

$$\frac{1}{(m_{B'}a)^3} = \frac{1}{(m_4a)^3}, \quad (6.4)$$

where the equality holds at the tree level for the choices of parameters in our action. The difference between am_4 and am_2 captures the discretization error. The fractional error in the hyperfine splitting due to this mismatch is

$$(a\Lambda_{\text{QCD}})^2 2am_2 \left[\frac{1}{(2am_4)^3} - \frac{1}{(2am_2)^3} \right]. \quad (6.5)$$

This error is plotted as a (green) dash-dot line on an X in Fig. 8. It would be added in quadrature with the error on the filled dot, if it were to be included in the total error. Again we take $\Lambda_{\text{QCD}} = 0.7$ GeV, but choosing $\Lambda_{\text{QCD}} = 0.5$ would cut these error bars in half. The error from Eq. (6.5) is small for the D_s splitting at the fine lattice spacing, but increasingly large and non-negligible at the coarse and medium-coarse lattice spacings; for the B_s splitting, the error is negligible.

Finally, we turn to the effects of the $O(\alpha_s)$ mistuning in c_B , which leads to an $O(\alpha_s)$ mismatch between $m_B a$ and $m_2 a$. Ideally, c_B should be adjusted so the coefficient of $\bar{h}^{(+)} i\boldsymbol{\sigma} \cdot \mathbf{B} h^{(+)}$ equals $Z_B/2m_2$, where Z_B is a coefficient with an anomalous dimension, such that $Z_B \bar{h}^{(+)} i\boldsymbol{\sigma} \cdot \mathbf{B} h^{(+)}$ is scale and scheme independent [49]. In practice, c_B is chosen in some approximation, in our case the tadpole-improved tree level of perturbation theory.

Given a value of c_B , our simulations produce

$$M_1^* - M_1 = \Delta_1 = \frac{4\lambda_2}{2m_B(c_B)}. \quad (6.6)$$

From Eq. (A26), we see that $1/am_B$ has a contribution $c_B/(1+m_0a)$. Hence, to include the leading correction to the hyperfine splitting, we shift

$$4\lambda_2 a \left[\frac{1}{2am_B(c_B)} \right] \rightarrow 4\lambda_2 a \left[\frac{1}{2am_B(c_B)} + \frac{c_B^{\text{ideal}} - c_B}{2(1+m_0a)} \right] \quad (6.7)$$

⁴ Other dimension-six and -seven operators are either redundant, loop-suppressed, or known to have small coefficients [23].

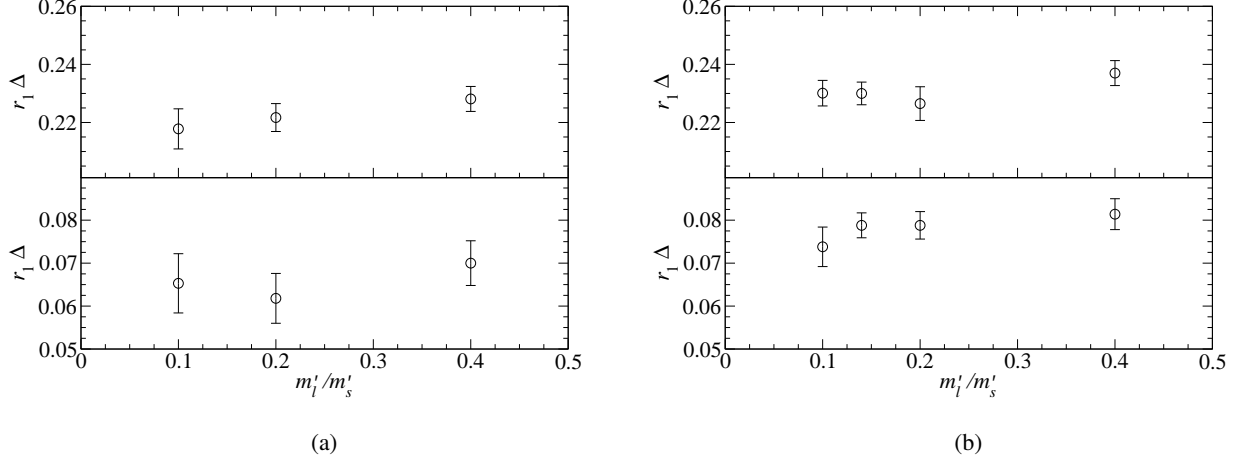


FIG. 7: The hyperfine splitting, in units of r_1 , versus the ratio of the light to strange sea-quark masses m'_l/m'_s on (a) fine and (b) coarse ensembles. Errors are the average 68% bootstrap error. The upper panel in each plot is for charm-like splittings and the lower panel is for bottom-like splittings. Values of κ are 0.127, 0.0923 for the fine ensembles and 0.122, 0.086 for coarse ensembles. Values of am'_q are 0.0272 and 0.0415 for the fine and coarse ensembles, respectively.

where c_B^{ideal} is the ideal choice. (Because loop corrections to $1/am_B$ depend on c_B , subleading corrections also exist.) To estimate the error in Δ_1 , we have to estimate $c_B^{\text{ideal}} - c_B$. In fact, Eq. (6.7) can also be used to shift the central value of the hyperfine splitting.

Reference [50] describes preliminary work on a calculation of the one-loop corrections to $c_B^{[1]}$, as a function of the bare quark mass. For all relevant values of $m_0 a$, the one-loop effects are a small correction to the tadpole-improved Ansatz $c_B = u_0^{-3}$, provided that u_0 is the average link in Landau gauge. On the coarse ensembles, we chose u_0 this way, and we can estimate the remaining correction directly from the calculation in Ref. [50]. Given further uncertainties from higher orders, we take this small correction as an uncertainty estimate. On the medium-coarse and fine ensembles, however, we chose u_0^4 to be the average plaquette. In those cases, the leading correction to c_B comes from,

$$c_B^{\text{ideal}} - c_B = u_{0,\text{LL}}^{-3} - u_{0,\text{plaq}}^{-3} \quad (6.8)$$

where the labels refer to “Landau-gauge link” and “plaquette.” Equation (6.8) leads to significant corrections to the hyperfine splitting, so we shift Δ_1 on the medium-coarse and fine ensembles by the amount corresponding to Eq. (6.7) and (6.8). These shifts put Δ_1 at the medium-coarse and fine lattice spacings on the same footing as those at the coarse spacing. Empirically, they flatten the lattice-spacing dependence.

For the medium-coarse and fine data, we use the values of u_0 given in Table XVI to calculate the shift described above. It is displayed in Fig. 8 as a (pink) star with a single-sided, positive error bar. To obtain an error bar corresponding to the one-loop correction to c_B in Ref. [50], we take $\alpha_s(0.09 \text{ fm}) = 1/3$ and use one-loop running to obtain values of α_s for the coarse and medium-coarse lattices. These corrections are shown in Fig. 8 as a (red) triangle with a solid error bar.

In summary, discretization errors in the hyperfine splitting are small at the fine lattice spacing; therefore, we take as our final results the splittings calculated on the fine lattice. In addition, since the effect of the leading $O(\alpha_s)$ mistuning of c_B can be quantified, we shift our final central values by this amount. All other discretization errors are included in our final error. We convert our results to physical units using the values of r_1/a and r_1 as listed in Table I. After including the error from the units conversion in the total, our final results for the hyperfine splittings are

$$\Delta_{D_s} = 145 \pm 15 \text{ MeV} \quad (6.9)$$

$$\Delta_{B_s} = 40 \pm 9 \text{ MeV} \quad (6.10)$$

These results are in good agreement with the PDG values of $143.9 \pm 0.4 \text{ MeV}$ and $46.1 \pm 1.5 \text{ MeV}$, respectively.

C. The critical hopping parameter κ_{crit}

In principle, it is possible to carry out a suite of nonperturbative heavy-quark calculations without knowing κ_{crit} , but in practice κ_{crit} is useful. In particular, it enters the construction of improved bilinear and 4-quark operators via $m_0 a$ Eq. (2.5). It

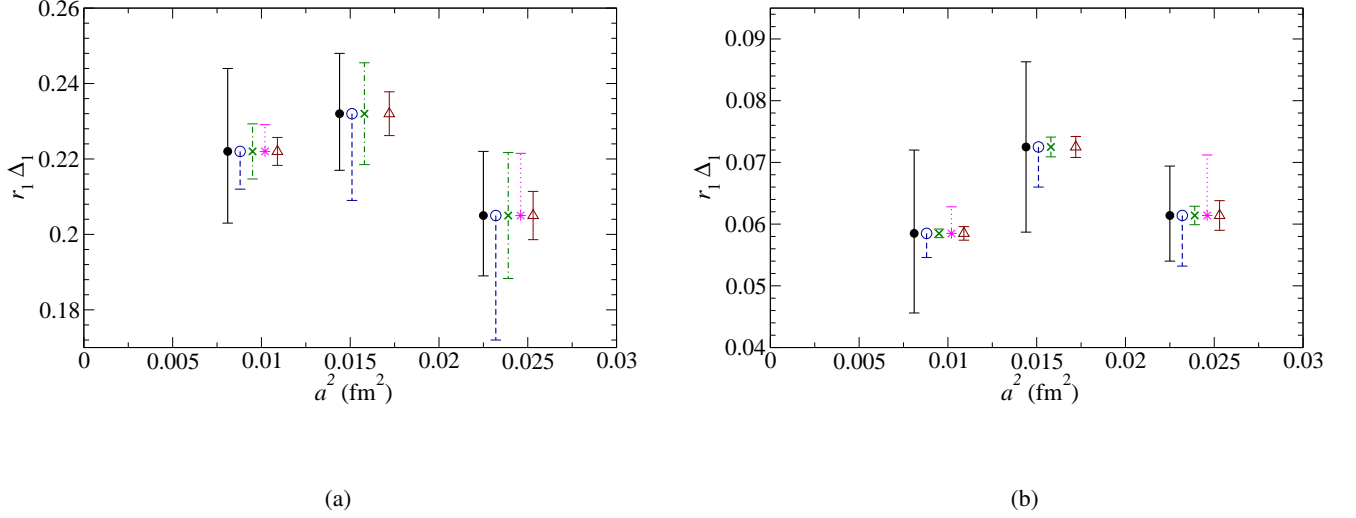


FIG. 8: Hyperfine splittings in r_1 units versus the squared lattice spacing a^2 (fm^2) for the (a) D_s meson and (b) B_s meson. Filled (black) dots with a solid error bar show the splitting with an error from all sources *except* discretization. Open (blue) circles with a dashed error bar show the splitting with an error that also includes discretization error effects in κ . (Green) X's with dash-dotted error bars show the estimated size of discretization effects from the lattice-continuum mismatch of the dimension-7 operator $\{i\sigma \cdot \mathbf{B}, \mathbf{D}^2\}$ — the errors are barely visible for the B_s system. (Pink) stars with a dotted error bar show the $O(\alpha_s)$ discretization error from the 1-loop mismatch between m_2 and m_B . For the difference between the $O(\alpha_s)$ discretization effects on the coarse lattice versus the fine and medium-coarse lattices, see the text.

also enters the computation of matching factors such as Z_V and Z_A [18]. Note that these all amount to small corrections, so we do not need a very precise determination of κ_{crit} . Equation (2.5) shows that it does not have to be much better determined than κ_c and κ_b .

A nonperturbative definition of κ_{crit} is the value of κ such that the mass of a pseudoscalar meson consisting of two Wilson quarks (with the clover action) vanishes. The computation of these light-light pseudoscalar meson masses shares code with the

TABLE XIV: Percent errors in the hyperfine splitting, $a\Delta_1$, of D_s *not* including discretization effects.

Uncertainty	Fine	Coarse	Medium-coarse
Statistical	2.2	1.9	1.9
κ tuning	(8.8, -7.5)	(4.0, -3.1)	(4.0, -2.7)
Valence m_s	0	0	0
Sea-quark masses	3.6	5.4	6.9
Total	(10, -9)	(7, -7)	(8, -8)

TABLE XV: Percent errors in the hyperfine splitting, $a\Delta_1$, of B_s *not* including discretization effects.

Uncertainty	Fine	Coarse	Medium-coarse
Statistical	9.5	4.0	5.6
κ tuning	(12, -11)	(17, -17)	(11, -10)
Valence m_s	0	0	0
Sea-quark masses	17	7.8	2.6
Total	(23, -22)	(19, -19)	(13, -12)

TABLE XVI: Tadpole-improvement factors for the estimate of the $O(\alpha_s)$ discretization error shown in Fig. 8.

ensemble	$u_{0,\text{plaquette}}$	$u_{0,\text{Landau}}$
fine (0.0062, 0.031)	0.878	0.854
medium-coarse (0.0097, 0.0484)	0.860	0.822

TABLE XVII: Values of κ_{crit} by ensemble. “ u_0 used” gives the origin of the u_0 value used in the κ_{crit} determination. κ_{crit} values are given in two columns. The first κ_{crit} column contains values which were determined by a fit. The second κ_{crit} column contains values which were estimated from fitted values at the same (approximate) lattice spacing. The last column gives the fit method used in the determination, explained in the text.

Lattice	(am'_l, am'_s)	u_0 used	κ_{crit}		
			Iterated fit	Direct fit	Estimated
Fine	(0.0031, 0.031)	Landau-gauge link			0.1372
	(0.0062, 0.031)	Landau-gauge link	0.1372		
	(0.0062, 0.031)	plaquette	0.1391		
	(0.0124, 0.031)	Landau-gauge link	0.1372		
Coarse	(0.005, 0.050)	Landau-gauge link			0.1379
	(0.007, 0.050)	Landau-gauge link			0.1379
	(0.010, 0.050)	Landau-gauge link	0.1379		
	(0.020, 0.050)	Landau-gauge link	0.1378		
	(0.030, 0.050)	Landau-gauge link	0.1377		
Medium-coarse	(0.0097, 0.0484)	plaquette		0.1424	
	(0.0194, 0.0484)	plaquette		0.1424	
	(0.0290, 0.0484)	plaquette		0.1423	

work reported here and in Ref. [8], and it is convenient to report the analysis here. The value of κ_{crit} depends on u_0 via our choice of clover coupling, $c_B = c_E = u_0^{-3}$. In this and other work [3–8], u_0 has been set sometimes from the average plaquette and sometimes from the average link in Landau gauge. The prescription for u_0 used in each κ_{crit} determination is given in column four of Table XVII.

The determination of κ_{crit} is carried out on a subset of the available configurations, 50–100 configurations for the fine ensembles and 400–600 for the coarse and medium-coarse. We compute two-point correlators for a range of κ that yields meson masses of about $M_{\text{PS}} = 450\text{--}900$ MeV on the fine ensembles, $650\text{--}1100$ MeV on the coarse ensembles, and $550\text{--}950$ MeV on the medium-coarse ensembles. It is impractical to push to lower M_{PS} due to exceptional configurations. M_{PS} is a function of the quark mass, which we parametrize as the tree-level, tadpole-improved kinetic or rest mass. In the relevant region, $m_{1,2}a = m_0a[1 - \frac{1}{2}m_0a] + O((m_0a)^3)$, so both pertain equally well. The meson masses can be fit to a polynomial ansatz

$$a^2 M_{\text{PS}}^2(\kappa) = A + B a m_2(\kappa, \kappa_{\text{crit}}) + C a^2 m_2^2(\kappa, \kappa_{\text{crit}}) \quad (6.11)$$

(or m_1 instead of m_2), where $A = 0$ when κ_{crit} is correctly adjusted.

We use two techniques to determine κ_{crit} . One method starts with a reasonable value of κ_{crit} and fits Eq. (6.11) to obtain A , B , and C , which depend implicitly on κ_{crit} . A better trial value of κ_{crit} is chosen, and the process is iterated until a κ_{crit} is found such that $A = 0$. We call this the “iterated fit”. The second method freezes A to zero, and then B , C , and κ_{crit} are the fit parameters. We call this the “direct fit”. On several ensembles the κ_{crit} values were simply estimated from the other ensembles with the same (approximate) lattice spacing, these are labeled as “estimated”.

Table XVII contains our results for κ_{crit} , indicating the method used. The table does not include error bars for κ_{crit} , but we believe that the results are correct to the number of significant figures shown, even though the range of M_{PS} is high. We carried out several tests to verify this accuracy. We compared linear iterated fits [i.e., $C = 0$ in Eq. (6.11)] to the baseline quadratic. We also compared direct fits with and without the (continuum) chiral log. These test show that higher order or log contributions do not alter our values of κ_{crit} significantly. We fit comparable data with staggered valence quarks allowing $(m_0a)_{\text{crit}} \neq 0$, thereby testing whether a range of such large M_{PS} skews the results. None of these tests suggests an error larger than a few in the fourth digit. Such errors are negligible compared to those for κ_c and κ_b —see Tables XII and XIII—when forming m_0a with Eq. (2.5).

VII. SUMMARY AND OUTLOOK

An accurate and precise determination of κ_c and κ_b is important for all calculations using the Fermilab action [3–8]. In this analysis, the error on κ_b is dominated by statistics, and the error on κ_c receives approximately equal contributions from statistics and discretization effects. These errors play a significant role on quantities as diverse as D - and B -meson decay constants [3] and the quarkonium hyperfine splitting [8]. Our final results for κ_c and κ_b are given in Table XIII.

Another ingredient that is useful for matrix elements [3–5] is the additive renormalization of the bare quark mass or, equivalently, κ_{crit} . The improvement and matching of the operators needed to compute these matrix elements depends mildly on κ_{crit} via m_0a [18]. Our final results for κ_{crit} are given in Table XVII.

The key ingredient needed to determine κ_c and κ_b is a computation of the pseudoscalar and vector heavy-strange meson masses. These can be combined to yield the hyperfine splitting for D_s and B_s mesons. Our final results for the hyperfine

splittings are given in Eqs. (6.9) and (6.10). Both are in good agreement with the corresponding PDG averages. These results bolster confidence in the tuning of κ_c and κ_b , as well as the choice $c_B = u_0^{-3}$. Further tests of these choices come from related calculations of the quarkonium spectrum [8]. With detailed attention given to the connection between action parameters and mass splittings, those results are found to be consistent with experiment within the expected uncertainties.

Improved determinations of κ_c , κ_b , and κ_{crit} for the medium-coarse, coarse, and fine ensembles are underway with higher statistics, as well as calculations on the new superfine ($a \approx 0.06$ fm), and ultrafine ($a \approx 0.045$ fm) lattices. The increased statistics will also allow us to use higher momentum data and fit to the $O(p^4)$ terms in the dispersion relation. Refinements in the determination and use of r_1/a are allowing for a better understanding of sea-quark effects which will be needed as the statistical error on aM_2 decreases. We are also investigating the use of twisted boundary conditions [51] which will allow us to obtain data points at lower momenta.

As uncertainties in M_2 and M_1 decrease, there will be a need for a better understanding of the chiral behavior of these masses. One-loop, $O(\Lambda/m_Q)$ chiral perturbation theory results exist for continuum QCD [47]. The extension to staggered chiral perturbation theory should be straightforward, and would allow us to extrapolate the light-valence mass to the physical up/down quark mass and determine the hyperfine splittings of the B^\pm and D^\pm mesons. In this paper, we have included the partially quenched expression for the hyperfine splitting in Appendix D, since it is useful in estimating uncertainties from the unphysical sea-quark masses.

In addition, tuned values of κ_c , κ_b , and κ_{crit} combined with one-loop (lattice) perturbation theory can yield determinations of the pole masses m_1 and m_2 for both charmed and bottom quarks⁵, which can be converted to the potential-subtracted, $\overline{\text{MS}}$, and other schemes [6]. Quark masses combined with staggered chiral perturbation theory for the B^\pm and D^\pm mesons, can yield *ab initio* calculations of HQET matrix elements [22, 52], which are used to calculate the Cabibbo-Kobayashi-Maskawa matrix element $|V_{cb}|$ via inclusive decay measurements. Finally, improved determinations of the oscillating-state energy E^p could make determinations of the experimentally accessible masses of the positive parity states, $D_{s0}^*(2317)$ and $D_{s1}(2460)$ [53] a viable option [54].

Acknowledgments

Computations for this work were carried out on facilities of the USQCD Collaboration, which are funded by the Office of Science of the U.S. Department of Energy. This work was supported in part by the U.S. Department of Energy under Grants No. DE-FC02-06ER41446 (C.D., L.L.), No. DE-FG02-91ER40661 (S.G.), No. DE-FG02-91ER40677 (A.X.K., E.G., R.T.E.), No. DE-FG02-91ER40628 (C.B, E.D.F.), No. DE-FG02-04ER-41298 (D.T.); the National Science Foundation under Grants No. PHY-0555243, No. PHY-0757333, No. PHY-0703296 (C.D., L.L.), No. PHY-0757035 (R.S.), No. PHY-0704171 (J.E.H.) and No. PHY-0555235 (E.D.F.); URA visiting scholars awards (E.G., R.T.E.), and the M. Hildred Blewett Scholarship of the American Physical Society (E.D.F.). This manuscript has been co-authored by an employee of Brookhaven Science Associates, LLC, under Contract No. DE-AC02-98CH10886 with the U.S. Department of Energy. R.S.V. acknowledges support from BNL via the Goldhaber Distinguished Fellowship. Fermilab is operated by Fermi Research Alliance, LLC, under Contract No. DE-AC02-07CH11359 with the U.S. Department of Energy.

Appendix A: Discretization Error in the Kinetic Meson Mass

In this appendix, we present a semi-quantitative estimation of the discretization error in the kinetic mass of heavy-light hadrons. We use a formalism that applies when both quarks are non-relativistic, even though this approximation is not good for the light quark in a heavy-light meson. A posteriori, we examine two ways to re-interpret the resulting formula for a relativistic light quark. Both estimates are numerically the same, so we proceed to use the formula in Sec. V B.

In what follows, the generalized masses m_1, m_2, m_4 and the coefficient w_4 are used to describe the discretization errors. Expressions for them when using the Fermilab action are in Refs. [14] or [23] and are given at the end of this appendix for convenience. We assume that the light quark (s) has a mass in lattice units $m_s a \ll 1$ and makes no significant contribution to the discretization error.

The bound state's kinetic mass can be read off from its kinetic energy (by definition). It will have a kinematic contribution, from the constituents' kinetic energy, and a dynamical contribution, from the interaction that binds the constituents. We consider each in turn.

⁵ The determination of the quark mass from m_1 requires a non-perturbative calculation of the binding energy as defined by $M_1 - m_1$ [6].

1. Contributions from constituents' kinetic energy

The hadron of interest is a heavy-strange meson, a bound state of a heavy quark Q (momentum \mathbf{Q}) and a strange antiquark s (momentum \mathbf{s}). The non-relativistic kinetic energy is

$$T = m_{1Q} + \frac{\mathbf{Q}^2}{2m_{2Q}} - \frac{(\mathbf{Q}^2)^2}{8m_{4Q}^3} - \frac{1}{6}w_{4Q}a^3 \sum_i Q_i^4 + m_{1s} + \frac{\mathbf{s}^2}{2m_{2s}} - \frac{(\mathbf{s}^2)^2}{8m_{4s}^3} - \frac{1}{6}w_{4s}a^3 \sum_i s_i^4. \quad (\text{A1})$$

The binding energy is communicated to the bound-state kinetic mass via the terms quartic in the momenta and via corrections to the potential, given below. In general, the lattice breaks relativistic invariance, so $m_1 \neq m_2 \neq m_4$, $w_4 \neq 0$. Re-writing the kinetic energy in center-of-mass coordinates

$$\mathbf{Q} = \frac{m_{2Q}}{m_{2Q} + m_{2s}} \mathbf{P} + \mathbf{p}, \quad (\text{A2})$$

$$\mathbf{s} = \frac{m_{2s}}{m_{2Q} + m_{2s}} \mathbf{P} - \mathbf{p}, \quad (\text{A3})$$

$$\mathbf{P} = \mathbf{Q} + \mathbf{s}, \quad (\text{A4})$$

$$\mathbf{p} = \frac{m_{2s}\mathbf{Q} - m_{2Q}\mathbf{s}}{m_{2Q} + m_{2s}}, \quad (\text{A5})$$

one finds

$$T = m_{1Q} + m_{1s} + \frac{\mathbf{P}^2}{2(m_{2Q} + m_{2s})} + \frac{\mathbf{p}^2}{2\mu_2} - \frac{\mathbf{P}^2 \mathbf{p}^2 + 2(\mathbf{P} \cdot \mathbf{p})^2}{4(m_{2Q} + m_{2s})^2} \left[\frac{m_{2Q}^2}{m_{4Q}^3} + \frac{m_{2s}^2}{m_{4s}^3} \right] - a^3 \sum_i \frac{P_i^2 p_i^2}{(m_{2Q} + m_{2s})^2} (w_{4Q}m_{2Q}^2 + w_{4s}m_{2s}^2) + \dots, \quad (\text{A6})$$

$$\frac{1}{\mu_2} = \frac{1}{m_{2Q}} + \frac{1}{m_{2s}}. \quad (\text{A7})$$

The only quartic terms shown are those quadratic in \mathbf{P} ; the omitted terms are not smaller; they just do not contribute to the bound state's kinetic energy. The objective is to collect all terms quadratic in \mathbf{P} , because their overall coefficient will yield the bound state's kinetic mass.

2. Contribution from the interaction: Breit equation

To obtain the two-particle system's potential energy, one has to work out the scattering amplitude from one-gluon exchange, obtaining an expression called the Breit equation [46, 55].

In momentum space, for the color-singlet channel

$$V(\mathbf{K}) = -C_F g^2 D_{\mu\nu}(K) \mathcal{N}_Q(\mathbf{Q} + \mathbf{K}) \bar{u}(\xi', \mathbf{Q} + \mathbf{K}) \Lambda_Q^\mu(Q + K, Q) u(\xi, \mathbf{Q}) \mathcal{N}_Q(\mathbf{Q}) \times \mathcal{N}_s(\mathbf{s}) \bar{v}(\xi, \mathbf{s}) \Lambda_s^\nu(s, s - K) v(\xi', \mathbf{s} - \mathbf{K}) \mathcal{N}_s(\mathbf{s} - \mathbf{K}), \quad (\text{A8})$$

where $D_{\mu\nu}$ is the (lattice) gluon propagator, Λ_q^μ is the lattice vertex function (for $q = Q, s$), and \mathcal{N}_q is an external-line factor needed with the normalization conditions on spinors employed here [14, 23]. (In continuum field theory, $\mathcal{N} = \sqrt{m/E}$.)

To the accuracy needed here, the gluon propagator can be replaced with the continuum propagator. The heavy-quark line is

$$J_Q^4 = \mathcal{N}_Q(\mathbf{Q} + \mathbf{K}) \bar{u}(\xi', \mathbf{Q} + \mathbf{K}) \Lambda_Q^4(Q + K, Q) u(\xi, \mathbf{Q}) \mathcal{N}_Q(\mathbf{Q}) = \bar{u}(\xi', \mathbf{0}) \left[1 - \frac{\mathbf{K}^2 - 2i\boldsymbol{\Sigma} \cdot (\mathbf{K} \times \mathbf{Q})}{8m_{EQ}^2} + \dots \right] u(\xi, \mathbf{0}), \quad (\text{A9})$$

$$J_Q = \mathcal{N}_Q(\mathbf{Q} + \mathbf{K}) \bar{u}(\xi', \mathbf{Q} + \mathbf{K}) \Lambda_Q(Q + K, Q) u(\xi, \mathbf{Q}) \mathcal{N}_Q(\mathbf{Q}) = -i\bar{u}(\xi', \mathbf{0}) \left[\frac{\mathbf{Q} + \frac{1}{2}\mathbf{K}}{m_{2Q}} + \frac{i\boldsymbol{\Sigma} \times \mathbf{K}}{2m_{BQ}} + \dots \right] u(\xi, \mathbf{0}), \quad (\text{A10})$$

and, to the extent that the strange antiquark is non-relativistic, one has a similar expression for the antiquark line $J_s^\nu = \mathcal{N}_s(\mathbf{s}) \bar{v}(\xi, \mathbf{s}) \Lambda_s^\nu(s, s - K) v(\xi', \mathbf{s} - \mathbf{K}) \mathcal{N}_s(\mathbf{s} - \mathbf{K})$.

In Coulomb gauge,

$$D_{44}(K) = \frac{1}{\mathbf{K}^2}, \quad D_{ij}(K) = \frac{1}{K^2} \left(\delta^{ij} - \frac{K^i K^j}{\mathbf{K}^2} \right), \quad (\text{A11})$$

and the other components vanish. Thus, noting that $K_4 = i[(\mathbf{Q} + \mathbf{K})^2 - \mathbf{Q}^2]/2m_Q$ is subleading,

$$V(\mathbf{K}) = -C_F g^2 \left[\frac{1}{\mathbf{K}^2} - \left(\frac{1}{8m_{EQ}^2} + \frac{1}{8m_{Es}^2} \right) - \frac{1}{m_{2Q}m_{2s}} \left(\mathbf{Q} \cdot \mathbf{s} - \frac{\mathbf{Q} \cdot \mathbf{K} \mathbf{K} \cdot \mathbf{s}}{\mathbf{K}^2} \right) \frac{1}{\mathbf{K}^2} \right] \\ + \text{spin-dependent terms.} \quad (\text{A12})$$

Let us discuss each part of the bracket in turn. The leading term yields, after Fourier transforming to position space, the $1/r$ potential. The second yields a contact term proportional to $\delta(\mathbf{r})$: it is a relativistic correction to the bound state's rest mass, so it is of no further interest here. Similarly, the spin-dependent terms do not contribute to the bound state's kinetic energy, so they are not written out. The remaining exhibited contributions do contribute to the bound state's kinetic energy, when \mathbf{Q} and \mathbf{s} are eliminated in favor of \mathbf{P} and \mathbf{p} .

Next we Fourier transform from \mathbf{K} to \mathbf{r} using

$$\int \frac{d^3 K}{(2\pi)^3} \frac{e^{i\mathbf{r} \cdot \mathbf{K}}}{\mathbf{K}^2} = \frac{1}{4\pi r}, \quad (\text{A13})$$

$$\int \frac{d^3 K}{(2\pi)^3} \frac{K_i K_j e^{i\mathbf{r} \cdot \mathbf{K}}}{(\mathbf{K}^2)^2} = \frac{1}{2} (\delta_{ij} + r_i \nabla_j) \int \frac{d^3 K}{(2\pi)^3} \frac{e^{i\mathbf{r} \cdot \mathbf{K}}}{\mathbf{K}^2}. \quad (\text{A14})$$

Following with the substitution of \mathbf{P} and \mathbf{p} for \mathbf{Q} and \mathbf{s} this yields

$$V(\mathbf{r}, \mathbf{P}, \mathbf{p}) = -\frac{C_F \alpha_s}{r} \left[1 - \frac{\mathbf{P}^2}{2(m_{2Q} + m_{2s})^2} \right] - r_i \nabla_j \frac{C_F \alpha_s}{r} \frac{P_i P_j}{2(m_{2Q} + m_{2s})^2} + \dots, \quad (\text{A15})$$

where the omitted terms do not influence the bound state's kinetic energy.

Note that \mathbf{K} changes \mathbf{p} but not \mathbf{P} , so \mathbf{r} is conjugate to \mathbf{p} . To take expectation values, we use the virial theorem

$$\langle r_i \nabla_j V(\mathbf{r}) \rangle = \frac{\langle p_i p_j \rangle}{\mu_2}, \quad (\text{A16})$$

so the total energy of the bound state, $E(\mathbf{P}) = \langle T + V \rangle$, is

$$E(\mathbf{P}) = m_{1Q} + m_{1s} + \frac{\langle \mathbf{p}^2 \rangle}{2\mu_2} - \left\langle \frac{C_F \alpha_s}{r} \right\rangle \\ + \frac{\mathbf{P}^2}{2(m_{2Q} + m_{2s})} \left[1 - \frac{\langle \mathbf{p}^2 \rangle}{2\mu_2(m_{2Q} + m_{2s})} + \frac{1}{(m_{2Q} + m_{2s})} \left\langle \frac{C_F \alpha_s}{r} \right\rangle \right] \\ + \frac{\mathbf{P}^2}{2(m_{2Q} + m_{2s})^2} \frac{\langle \mathbf{p}^2 \rangle}{2\mu_2} \left[1 - \mu_2 \left(\frac{m_{2Q}^2}{m_{4Q}^3} + \frac{m_{2s}^2}{m_{4s}^3} \right) \right] \\ + \frac{P_i P_j}{(m_{2Q} + m_{2s})^2} \frac{\langle p_i p_j \rangle}{2\mu_2} \left[1 - \mu_2 \left(\frac{m_{2Q}^2}{m_{4Q}^3} + \frac{m_{2s}^2}{m_{4s}^3} \right) \right] \\ - a^3 \sum_i \frac{P_i^2 \langle p_i^2 \rangle}{(m_{2Q} + m_{2s})^2} (w_{4Q} m_{2Q}^2 + w_{4s} m_{2s}^2) + \dots \quad (\text{A17})$$

The first line of Eq. (A17) shows the binding energy adding to the quarks' rest masses to form the bound state's rest mass,

$$M_1 = m_{1Q} + m_{1s} + \frac{\langle \mathbf{p}^2 \rangle}{2\mu_2} - \left\langle \frac{C_F \alpha_s}{r} \right\rangle. \quad (\text{A18})$$

The second line shows the same binding energy modifying the kinetic energy. The remaining terms are discretization errors. In general they are a bit messy, but they simplify for the S -wave states we use to tune κ . Then $\langle p_i p_j \rangle = \frac{1}{3} \delta_{ij} \langle \mathbf{p}^2 \rangle$, whence

$$E(\mathbf{P}) = M_1 + \frac{\mathbf{P}^2}{2M_2} + \dots, \quad (\text{A19})$$

where

$$\begin{aligned}
M_2 &= m_{2Q} + m_{2s} + \frac{\langle \mathbf{p}^2 \rangle}{2\mu_2} - \left\langle \frac{C_F \alpha_s}{r} \right\rangle \\
&+ \frac{5}{3} \frac{\langle \mathbf{p}^2 \rangle}{2\mu_2} \left[\mu_2 \left(\frac{m_{2Q}^2}{m_{4Q}^3} + \frac{m_{2s}^2}{m_{4s}^3} \right) - 1 \right] + \frac{4}{3} a^3 \frac{\langle \mathbf{p}^2 \rangle}{2\mu_2} \mu_2 (w_{4Q} m_{2Q}^2 + w_{4s} m_{2s}^2) + \dots
\end{aligned} \tag{A20}$$

The last line exhibits the discretization errors, which would vanish if $m_4 = m_2$, $w_4 = 0$.

The error can be re-written

$$\delta M_2 = \frac{1}{3} \frac{\langle \mathbf{p}^2 \rangle}{2\mu_2} \left\{ 5 \left[\mu_2 \left(\frac{m_{2Q}^2}{m_{4Q}^3} + \frac{m_{2s}^2}{m_{4s}^3} \right) - 1 \right] + 4a\mu_2 [w_{4Q}(m_{2Q}a)^2 + w_{4s}(m_{2s}a)^2] \right\}, \tag{A21}$$

which is equivalent to Eq. (14) of Ref. [46]. Note that the error ends up being proportional to the internal kinetic energy of the bound state, $\langle \mathbf{p}^2 \rangle / 2\mu_2$.

3. Relativistic light degrees of freedom

For asqtad light quarks, the discretization errors are $O(\alpha_s m_s^2 a^2)$ and $O(m_s^4 a^4)$. So, for a semi-quantitative estimate of the discretization error, it should be safe to assume $m_{4s} = m_{2s} = m_{1s} = m_s$, $a^3 w_{4s} = 0$. Equation (A21) is then

$$\delta M_2 = \frac{1}{3m_{2Q}} \frac{\langle \mathbf{p}^2 \rangle}{2\mu_2} \mu_2 \left[5 \left(\frac{m_{2Q}^2}{m_{4Q}^3} - 1 \right) + 4w_{4Q}(m_{2Q}a)^3 \right]. \tag{A22}$$

To use this formula we need a value for $\langle \mathbf{p}^2 \rangle$, and we consider two possibilities. The first is to replace $\langle \mathbf{p}^2 \rangle$ with $\bar{\Lambda}^2$. The reduced mass μ_2 then cancels, yielding a sensible limit even when $m_s \rightarrow 0$. The second is to replace the non-relativistic kinetic energy $\langle \mathbf{p}^2 \rangle / 2\mu_2$ with a relativistic version, namely $\bar{\Lambda}$. If we take a constituent quark mass $m_s = \frac{1}{2}\bar{\Lambda}$, then this discretization-error estimate equals that of the first approach to $O(m_s/m_Q)$.

4. The generalized masses and w_4

General tree-level expressions for the quark masses and w_4 were originally given in Ref. [14] and succinctly recapitulated in Ref. [23]. For convenience we give them here with parameters $\zeta = 1 = r_s$ as in our simulations

$$m_0 a = \frac{1}{u_0} \left(\frac{1}{2\kappa} - \frac{1}{2\kappa_{\text{crit}}} \right), \tag{A23}$$

$$m_1 a = \ln(1 + m_0 a) \tag{A24}$$

$$\frac{1}{m_2 a} = \frac{2}{m_0 a(2 + m_0 a)} + \frac{1}{1 + m_0 a}, \tag{A25}$$

$$\frac{1}{m_B a} = \frac{2}{m_0 a(2 + m_0 a)} + \frac{c_B}{1 + m_0 a}, \tag{A26}$$

$$\frac{1}{4m_E^2 a^2} = \frac{1}{[m_0 a(2 + m_0 a)]^2} + \frac{c_E}{m_0 a(2 + m_0 a)}, \tag{A27}$$

$$\frac{1}{m_4^3 a^3} = \frac{8}{[m_0 a(2 + m_0 a)]^3} + \frac{4 + 8(1 + m_0 a)}{[m_0 a(2 + m_0 a)]^2} + \frac{1}{(1 + m_0 a)^2}, \tag{A28}$$

$$w_4 = \frac{2}{m_0 a(2 + m_0 a)} + \frac{1}{4(1 + m_0 a)}. \tag{A29}$$

These expressions and Eq. (A22) are used to obtain Table IX.

Appendix B: Tables of the kinetic mass

In this appendix, we tabulate values of the pseudoscalar, vector, and spin-averaged kinetic mass, aM_2 , aM_2^* , and \overline{M}_2 , respectively. Values are given for all combinations of κ and am'_q on the ensembles used for tuning κ . χ^2/dof and the p value, one minus the χ^2 cumulative distribution [45], from the dispersion relation fits are also given.

	κ	aM_2	aM_2^*	\overline{M}_2	χ^2/dof (p)	
					aM_2	aM_2^*
$am'_q = 0.0272$	0.090	2.30(17)	2.31(25)	2.31(21)	0.21 (0.81)	0.24 (0.79)
	0.0923	2.19(15)	2.22(22)	2.21(19)	0.22 (0.80)	0.35 (0.71)
	0.093	2.16(14)	2.19(22)	2.18(18)	0.22 (0.80)	0.37 (0.69)
	0.1256	0.860(19)	0.936(42)	0.917(32)	0.09 (0.92)	0.14 (0.87)
	0.127	0.819(15)	0.912(39)	0.889(30)	0.36 (0.70)	0.00 (1.0)
$am'_q = 0.031$	0.0923	2.22(14)	2.22(21)	2.22(18)	0.18 (0.84)	0.31 (0.73)
	0.1256	0.871(18)	0.947(38)	0.928(30)	0.14 (0.87)	0.16 (0.85)
	0.127	0.828(15)	0.918(37)	0.895(29)	0.40 (0.67)	0.00 (1.0)

TABLE XVIII: The kinetic meson mass for bottom- and charm-type mesons on the (0.0062, 0.031) fine ensemble from fits to $E^2(\mathbf{p}) - E^2(\mathbf{0})$ using $|\mathbf{n}| \leq \sqrt{3}$. Fits are done to obtain aM_2 and aM_2^* and the results are then spin averaged. Uncertainties are the average 68% bootstrap error. χ^2/dof with the p value in parentheses is also given. The p value is one minus the χ^2 cumulative distribution [45].

	κ	aM_2	aM_2^*	\overline{M}_2	χ^2/dof (p)	
					aM_2	aM_2^*
$am'_q = 0.03$	0.074	3.78(49)	3.64(54)	3.67(50)	1.12 (0.33)	0.17 (0.84)
	0.086	2.93(21)	3.03(33)	3.01(29)	0.28 (0.76)	0.21 (0.81)
	0.093	2.50(14)	2.66(24)	2.62(21)	0.05 (0.95)	0.11 (0.90)
	0.119	1.263(16)	1.402(43)	1.368(34)	0.84 (0.43)	0.20 (0.82)
	0.122	1.132(17)	1.270(46)	1.236(37)	0.35 (0.70)	0.34 (0.71)
	0.124	1.038(16)	1.161(43)	1.130(33)	0.28 (0.76)	0.52 (0.60)
$am'_q = 0.0415$	0.074	3.66(35)	3.75(53)	3.73(48)	0.26 (0.77)	0.23 (0.79)
	0.086	2.99(19)	3.09(28)	3.06(25)	0.46 (0.63)	0.48 (0.62)
	0.093	2.57(13)	2.75(25)	2.70(21)	0.14 (0.87)	0.31 (0.73)
	0.119	1.292(15)	1.456(41)	1.415(33)	0.88 (0.41)	0.38 (0.69)
	0.122	1.157(17)	1.310(44)	1.272(36)	0.19 (0.83)	0.24 (0.79)
	0.124	1.065(15)	1.200(43)	1.166(34)	0.15 (0.86)	0.47 (0.63)

TABLE XIX: Same as Table XVIII but for mesons on the (0.007, 0.050) coarse ensemble.

	κ	$\chi^2/\text{dof} (p)$				
		aM_2	aM_2^*	$a\bar{M}$	aM_2	aM_2^*
$am'_q = 0.0484$	0.070	4.54(32)	4.53(45)	4.53(41)	0.55 (0.58)	0.78 (0.46)
	0.080	3.79(19)	3.77(27)	3.78(24)	0.54 (0.58)	1.19 (0.31)
	0.115	1.747(25)	1.825(47)	1.805(37)	1.32 (0.27)	0.36 (0.70)
	0.125	1.304(12)	1.415(32)	1.387(26)	1.23 (0.29)	0.05 (0.95)
$am'_q = 0.0387$	0.070	4.47(35)	4.44(50)	4.44(46)	0.47 (0.63)	0.72 (0.49)
	0.080	3.73(21)	3.70(31)	3.71(28)	0.53 (0.59)	1.07 (0.34)
	0.115	1.725(28)	1.804(58)	1.784(47)	1.06 (0.43)	0.04 (0.96)
	0.125	1.282(13)	1.388(37)	1.361(29)	0.89 (0.41)	0.07 (0.93)

TABLE XX: Same as Table XVIII but for mesons on the (0.0097, 0.0484) medium-coarse ensemble.

Appendix C: Tables of $M_1 = E(0)$ and the hyperfine splitting

In this appendix, we tabulate the hyperfine splitting $a\Delta_1$ and $r_1\Delta_1$ discussed in Sec. VI B.

1. The hyperfine splitting in lattice units $a\Delta_1$

In this subsection, we tabulate values of $a\Delta_1$ relevant to the discussion in Sec. VI B of the uncertainty in the hyperfine splitting due to statistics, κ tuning, and the light valence mass.

	κ	ensemble	aM_1	aM_1^*	$a\Delta_1$	
$am'_q = 0.0272$	0.090	(0.0062, 0.031)	1.7387(13)	1.7546(19)	0.0158(15)	
	0.0923	(0.0031, 0.031)	1.6877(21)	1.7054(25)	0.0177(19)	
	0.0923	(0.0062, 0.031)	1.6870(13)	1.7037(20)	0.0167(16)	
	0.0923	(0.0124, 0.031)	1.6835(16)	1.7024(19)	0.0188(14)	
	0.1256	(0.0062, 0.031)	0.8408(8)	0.8968(16)	0.0561(15)	
	0.127	(0.0031, 0.031)	0.7944(9)	0.8534(19)	0.0590(19)	
	0.127	(0.0062, 0.031)	0.7946(7)	0.8544(15)	0.0599(13)	
	0.127	(0.0124, 0.031)	0.7901(7)	0.8514(11)	0.0613(12)	
	$am'_q = 0.031$	0.090	(0.0062, 0.031)	1.7441(13)	1.7601(17)	0.0159(14)
		0.0923	(0.0062, 0.031)	1.6926(12)	1.7093(18)	0.0167(14)
0.1256		(0.0062, 0.031)	0.8470(8)	0.9030(14)	0.0560(13)	
0.127		(0.0062, 0.031)	0.8009(7)	0.8606(14)	0.0597(12)	

TABLE XXI: Fine-ensemble values of the rest mass $M_1 = E(0)$ and hyperfine splitting Δ_1 . $am'_q = 0.0272$ and 0.031 . Uncertainties are the average 68% bootstrap error.

	κ	ensemble	aM_1	aM_1^*	$a\Delta_1$	
$am'_q = 0.0415$	0.074	(0.007, 0.050)	2.2394(22)	2.2618(25)	0.0224(09)	
	0.086	(0.005, 0.050)	1.9662(17)	1.9941(27)	0.0279(18)	
	0.086	(0.007, 0.050)	1.9644(17)	1.9943(21)	0.0299(11)	
	0.086	(0.010, 0.050)	1.9676(16)	1.9978(21)	0.0301(12)	
	0.086	(0.020, 0.050)	1.9584(16)	1.9891(21)	0.0307(14)	
	0.122	(0.005, 0.050)	1.0529(10)	1.1399(22)	0.0870(17)	
	0.122	(0.007, 0.050)	1.0520(7)	1.1393(17)	0.0873(15)	
	0.122	(0.010, 0.050)	1.0549(10)	1.1414(26)	0.0865(22)	
	0.122	(0.020, 0.050)	1.0446(9)	1.1339(16)	0.0894(16)	
	0.124	(0.007, 0.050)	0.9871(7)	1.0819(17)	0.0948(15)	
	$am'_q = 0.030$	0.074	(0.007, 0.050)	2.2241(26)	2.2466(29)	0.0225(11)
		0.086	(0.007, 0.050)	1.9488(21)	1.9787(25)	0.0299(14)
0.122		(0.007, 0.050)	1.0339(08)	1.1220(20)	0.0881(17)	

TABLE XXII: Same as Table XXI but for the coarse ensembles with $am'_q = 0.0415$ and 0.03 .

	κ	ensemble	aM_1	aM_1^*	$a\Delta_1$	
$am'_q = 0.0484$	0.076	(0.0097, 0.0484)	2.3192(27)	2.3472(36)	0.0280(17)	
	0.076	(0.0194, 0.0484)	2.3153(30)	2.3424(47)	0.0270(26)	
	0.076	(0.0290, 0.0484)	2.3137(23)	2.3445(21)	0.0308(16)	
	0.080	(0.0097, 0.0484)	2.2298(24)	2.2606(34)	0.0308(17)	
	0.122	(0.0097, 0.0484)	1.2427(8)	1.3390(21)	0.0963(19)	
	0.122	(0.0194, 0.0484)	1.2397(8)	1.3400(17)	0.1004(14)	
	0.122	(0.0290, 0.0484)	1.2364(7)	1.3402(17)	0.1038(14)	
	0.125	(0.0097, 0.0484)	1.1565(8)	1.2634(21)	0.1069(20)	
	$am'_q = 0.0387$	0.076	(0.0097, 0.0484)	2.3060(31)	2.3341(40)	0.0281(19)
		0.122	(0.0097, 0.0484)	1.2271(9)	1.3237(25)	0.0966(24)

TABLE XXIII: Same as Table XXI but for medium-coarse ensembles with $am'_q = 0.0484$ and 0.0387 .

2. The hyperfine splitting in physical units $r_1\Delta_1$

In this subsection, we tabulate values of $r_1\Delta_1$ relevant to the discussion in Sec. VI B of the dependence of the hyperfine splitting on the sea-quark masses.

	ensemble	$r_1\Delta_1$
$\kappa = 0.0923$	(0.0031, 0.031)	0.0653(69)
	(0.0062, 0.031)	0.0618(58)
	(0.0124, 0.031)	0.0700(52)
$\kappa = 0.127$	(0.0031, 0.031)	0.2178(69)
	(0.0062, 0.031)	0.2217(48)
	(0.0124, 0.031)	0.2281(43)

TABLE XXIV: Fine-ensemble values of the hyperfine splitting Δ_1 in units of r_1 . $am'_q = 0.0272$. Uncertainties are the average 68% bootstrap error.

	ensemble	$r_1\Delta_1$
$\kappa = 0.086$	(0.005, 0.050)	0.0738(46)
	(0.007, 0.050)	0.0788(29)
	(0.010, 0.050)	0.0788(32)
	(0.020, 0.050)	0.0814(36)
$\kappa = 0.122$	(0.005, 0.050)	0.2301(44)
	(0.007, 0.050)	0.2300(39)
	(0.010, 0.050)	0.2265(58)
	(0.020, 0.050)	0.2370(43)

TABLE XXV: Same as Table XXIV but for the coarse-ensembles with $am'_q = 0.0415$.

	ensemble	$r_1\Delta_1$
$\kappa = 0.076$	(0.0097, 0.0484)	0.0616(37)
	(0.0194, 0.0484)	0.0603(57)
	(0.0290, 0.0484)	0.0699(37)
$\kappa = 0.122$	(0.0097, 0.0484)	0.2117(41)
	(0.0194, 0.0484)	0.2244(30)
	(0.0290, 0.0484)	0.2357(39)

TABLE XXVI: Same as Table XXIV but for medium-coarse-ensembles with $am'_q = 0.0484$.

Appendix D: Partially quenched chiral perturbation theory for the heavy-light hyperfine splitting

For full (unquenched) QCD, Jenkins [47] has calculated the hyperfine splitting at one loop in heavy-meson chiral perturbation theory. It is not difficult to take her result (Eq. (A.10) of Ref. [47]) and extend it to partially quenched QCD. The further step of including staggered taste-violations (*i.e.*, doing staggered chiral perturbation theory) would also be fairly straightforward, but we do not take it here because the continuum partially quenched form is sufficient for estimating the small systematic effect due to the mistuning of sea quark masses. Unlike Jenkins, we neglect electromagnetic and isospin-violating effects.

At the quark-flow level, the relevant diagrams are the self-energy diagrams shown in Fig. 5(a) [left] of Ref. [56] (the “connected diagram”) and in Figs. 5(b),(c) [left] of Ref. [56] (the “disconnected diagram”).⁶ One simply needs to determine how much of Jenkins’s result comes from each of these two diagrams. This is accomplished by noting that, when the light valence quark is a u ($a = 1$ in Jenkins’s notation), an internal kaon only appears in the connected diagram, when the quark in the virtual loop is an s . This fixes the normalization of the connected diagram. Using the methods described in Refs. [56–58] (but dropping the taste violations and indeed the taste degree of freedom itself), the disconnected diagram is easily calculated. Its normalization can then be fixed so that it supplies the remainder of the $a = 1$ result in Ref. [47].

There are ample checks of this reasoning. First, the same normalizations must apply for any choice of the valence mass. The η contributes in each case only through the disconnected diagram, while the pion contributions come from both connected and disconnected diagrams for valence u or d ($a = 1, 2$), and must be absent for valence s ($a = 3$). Finally the contribution from the unphysical $s\bar{s}$ state, which appears in each diagram for $a = 3$, should cancel.

It is then immediate to write down the partially quenched version. Let the light valence quark be x , with mass m_x , and let the sea quarks be u, d, s with masses $m_u = m_d = m_l$ and m_s . With the light meson decay constant f normalized so that $f \approx f_\pi \approx 130$ MeV, the hyperfine splitting $M_x^* - M_x$ is given by

$$M_x^* - M_x = \Delta - \frac{\Delta g_\pi^2}{8\pi^2 f^2} \delta_{\log} + 2\Delta^{(\sigma)}(2m_l + m_s) + 2\Delta^{(a)}m_x, \quad (\text{D1})$$

where Δ is the splitting in the (three-flavor) chiral limit, and $\Delta^{(\sigma)}$ and $\Delta^{(a)}$ are LECs that start at order $1/m_Q$ in the heavy quark expansion. The non-analytic chiral logarithms δ_{\log} are

$$\delta_{\log} = \sum_{F=u,d,s} \ell(M_{xF}^2) - \frac{1}{3} R_X^{[2,2]}(\{m\}, \{\mu\}) \tilde{\ell}(M_X^2) - \frac{1}{3} \sum_{j=X,\eta} D_{j,X}^{[2,2]}(\{m\}, \{\mu\}) \ell(M_j^2). \quad (\text{D2})$$

Here M_X is the mass of the valence $x\bar{x}$ meson, and M_{xF} is the mass of the mixed valence-sea $x\bar{F}$ meson. The residue functions $R_j^{[n,k]}$ and $D_{j,i}^{[n,k]}$, as well as the chiral logarithm functions $\ell(m^2)$ and $\tilde{\ell}(m^2)$, are defined in Refs. [57, 58]. The term with the sum over F comes from the connected diagram, while those with the residue functions come from the disconnected diagram, which has a double pole at M_X^2 in the partially quenched case. The denominator ($\{m\}$) and numerator ($\{\mu\}$) mass sets are

$$\{m\} = \{M_X, M_\eta\}, \quad \{\mu\} = \{M_U, M_S\} \quad (\text{D3})$$

with M_U and M_S the masses of the $u\bar{u}$ and $s\bar{s}$ mesons, respectively.

-
- [1] C. T. H. Davies *et al.* [HPQCD, MILC, and Fermilab Lattice Collaborations], Phys. Rev. Lett. **92**, 022001 (2004) [arXiv:hep-lat/0304004];
[2] C. Aubin *et al.* [HPQCD, MILC, and UKQCD Collaborations], Phys. Rev. D **70**, 031504(R) (2004) [arXiv:hep-lat/0405022]; C. Aubin *et al.* [MILC Collaboration], Phys. Rev. D **70**, 114501 (2004) [arXiv:hep-lat/0407028].
[3] C. Aubin *et al.* [Fermilab Lattice, MILC, and HPQCD Collaborations], Phys. Rev. Lett. **95**, 122002 (2005) [arXiv:hep-lat/0506030].
C. Bernard *et al.* [Fermilab Lattice and MILC Collaborations], PoS **LATTICE2008**, 278 (2008) [arXiv:0904.1895 [hep-lat]].
[4] C. Aubin *et al.* [Fermilab Lattice, MILC, and HPQCD Collaborations], Phys. Rev. Lett. **94**, 011601 (2005) [arXiv:hep-ph/0408306];
M. Okamoto *et al.* [Fermilab Lattice and MILC Collaborations], Nucl. Phys. B Proc. Suppl. **140**, 461 (2005) [arXiv:hep-lat/0409116];
C. Bernard *et al.* [Fermilab Lattice and MILC Collaborations], Phys. Rev. D **79**, 014506 (2009) [arXiv:0808.2519 [hep-lat]]; J. A. Bailey *et al.* [Fermilab Lattice and MILC Collaborations], Phys. Rev. D **79**, 054507 (2009) [arXiv:0811.3640 [hep-lat]]; C. Bernard *et al.* [Fermilab Lattice and MILC Collaborations], Phys. Rev. D **80**, 034026 (2009) [arXiv:0906.2498 [hep-lat]].
[5] R. T. Evans *et al.* [Fermilab Lattice and MILC collaborations], PoS **LATTICE 2008** 052 (2008); R. T. Evans, E. Gámiz, A. El-Khadra and A.S. Kronfeld [Fermilab Lattice and MILC Collaborations], PoS **LATTICE 2009** 245 (2009) [arXiv:0911.5432 [hep-lat]].

⁶ One should ignore the solid square in each of the figures from Ref. [56] because it represents a current insertion, not relevant here.

- [6] E. D. Freeland, A. S. Kronfeld, J. N. Simone and R. S. Van de Water [Fermilab Lattice and MILC Collaborations], PoS **LAT2007**, 243 (2007) [arXiv:0710.4339 [hep-lat]].
- [7] I. F. Allison *et al.* [HPQCD and Fermilab Lattice Collaborations], Phys. Rev. Lett. **94**, 172001 (2005) [arXiv:hep-lat/0411027].
- [8] T. Burch *et al.* [Fermilab Lattice and MILC Collaborations], Phys. Rev. D **81**, 034508 (2010) [arXiv:0912.2701 [hep-lat]].
- [9] C. W. Bernard *et al.*, Phys. Rev. D **64**, 054506 (2001) [arXiv:hep-lat/0104002].
- [10] C. Aubin *et al.*, Phys. Rev. D **70**, 094505 (2004) [arXiv:hep-lat/0402030].
- [11] A. Bazavov *et al.*, Rev. Mod. Phys., to be published [arXiv:0903.3598 [hep-lat]].
- [12] C. W. Bernard *et al.*, Phys. Rev. D **62**, 034503 (2000) [arXiv:hep-lat/0002028]; R. Sommer, Nucl. Phys. B **411**, 839 (1994) [arXiv:hep-lat/9310022].
- [13] T. Blum *et al.*, Phys. Rev. D **55**, R1133 (1997) [arXiv:hep-lat/9609036]; K. Orginos and D. Toussaint [MILC Collaboration], Phys. Rev. D **59**, 014501 (1998) [arXiv:hep-lat/9805009]; J. F. Lagaë and D. K. Sinclair, Phys. Rev. D **59**, 014511 (1998) [arXiv:hep-lat/9806014]; G. P. Lepage, Phys. Rev. D **59**, 074502 (1999) [arXiv:hep-lat/9809157]; K. Orginos, D. Toussaint and R. L. Sugar [MILC Collaboration], Phys. Rev. D **60**, 054503 (1999) [arXiv:hep-lat/9903032]; C. W. Bernard *et al.* [MILC Collaboration], Phys. Rev. D **61**, 111502(R) (2000) [arXiv:hep-lat/9912018].
- [14] A. X. El-Khadra, A. S. Kronfeld and P. B. Mackenzie, Phys. Rev. D **55**, 3933 (1997) [arXiv:hep-lat/9604004].
- [15] B. Sheikholeslami and R. Wohlert, Nucl. Phys. B **259**, 572 (1985).
- [16] K. G. Wilson, in *New Phenomena in Subnuclear Physics*, edited by A. Zichichi (Plenum, New York, 1977).
- [17] A. S. Kronfeld, Phys. Rev. D **62**, 014505 (2000) [arXiv:hep-lat/0002008].
- [18] J. Harada, S. Hashimoto, K. I. Ishikawa, A. S. Kronfeld, T. Onogi and N. Yamada, Phys. Rev. D **65**, 094513 (2002) [Erratum-ibid. D **71**, 019903 (2005)] [arXiv:hep-lat/0112044]; J. Harada, S. Hashimoto, A. S. Kronfeld and T. Onogi, Phys. Rev. D **65**, 094514 (2002) [arXiv:hep-lat/0112045].
- [19] K. Symanzik, in *Recent Developments in Gauge Theories*, edited by G. 't Hooft *et al.* (Plenum, New York, 1980); in *Mathematical Problems in Theoretical Physics*, edited by R. Schrader *et al.* (Springer, New York, 1982); Nucl. Phys. B **226**, 187, 205 (1983).
- [20] G. P. Lepage and P. B. Mackenzie, Phys. Rev. D **48**, 2250 (1993) [arXiv:hep-lat/9209022].
- [21] B. P. G. Mertens, A. S. Kronfeld and A. X. El-Khadra, Phys. Rev. D **58**, 034505 (1998) [arXiv:hep-lat/9712024].
- [22] A. S. Kronfeld and J. N. Simone, Phys. Lett. B **490**, 228 (2000) [Erratum-ibid. B **495**, 441 (2000)] [arXiv:hep-ph/0006345].
- [23] M. B. Oktay and A. S. Kronfeld, Phys. Rev. D **78**, 014504 (2008) [arXiv:0803.0523 [hep-lat]].
- [24] M. G. Alford, W. Dimm, G. P. Lepage, G. Hockney and P. B. Mackenzie, Phys. Lett. B **361**, 87 (1995) [arXiv:hep-lat/9507010].
- [25] C. W. Bernard *et al.* [MILC Collaboration], Phys. Rev. D **58**, 014503 (1998) [arXiv:hep-lat/9712010]; M. Lüscher and P. Weisz, Commun. Math. Phys. **97**, 59 (1985) [Erratum-ibid. **98**, 433 (1985)]; M. Luscher and P. Weisz, Phys. Lett. B **158**, 250 (1985).
- [26] Y. Shamir, Phys. Rev. D **71**, 034509 (2005) [arXiv:hep-lat/0412014]; Phys. Rev. D **75**, 054503 (2007) [arXiv:hep-lat/0607007].
- [27] C. Bernard, Phys. Rev. D **73**, 114503 (2006) [arXiv:hep-lat/0603011].
- [28] C. Bernard, M. Golterman and Y. Shamir, Phys. Rev. D **77**, 074505 (2008) [arXiv:0712.2560 [hep-lat]].
- [29] S. Dürr, PoS **LAT2005**, 021 (2006) [arXiv:hep-lat/0509026]; S. R. Sharpe, PoS **LAT2006**, 022 (2006) [arXiv:hep-lat/0610094]; M. Golterman, PoS **CONFINEMENT8**, 014 (2008) [arXiv:0812.3110 [hep-ph]].
- [30] A. S. Kronfeld, PoS **LAT2007**, 016 (2007) [arXiv:0711.0699 [hep-lat]].
- [31] For m_s and r_1/a , we use the fitting methods described in Ref. [11] as applied to the data available in June, 2007 [32]. Specifically, to smooth r_1/a , $\ln(r_1/a)$ is fit to a polynomial in β and $2am'_l + am'_s$. Values of u_0 can also be found in this reference.
- [32] C. Bernard *et al.* [MILC Collaboration], PoS **LAT2007**, 137 (2007) [arXiv:0711.0021 [hep-lat]].
- [33] A. Gray, I. Allison, C. T. H. Davies, E. Gulez, G. P. Lepage, J. Shigemitsu and M. Wingate, Phys. Rev. D **72**, 094507 (2005) [arXiv:hep-lat/0507013].
- [34] C. Bernard *et al.* [MILC Collaboration], PoS **LAT2005**, 025 (2006) [arXiv:hep-lat/0509137].
- [35] C. Bernard *et al.*, PoS **LAT2007**, 090 (2007) [arXiv:0710.1118 [hep-lat]].
- [36] C. T. H. Davies, E. Follana, I. D. Kendall, G. P. Lepage and C. McNeile, [arXiv:0910.1229 [hep-lat]].
- [37] D. P. Menscher, “Charmonium and charmed mesons with improved lattice QCD,” (University of Illinois Ph. D. thesis, 2005).
- [38] J. L. Richardson, Phys. Lett. B **82**, 272 (1979).
- [39] M. Wingate, J. Shigemitsu, C. T. H. Davies, G. P. Lepage and H. D. Trottier, Phys. Rev. D **67**, 054505 (2003) [arXiv:hep-lat/0211014].
- [40] M. F. L. Golterman, Nucl. Phys. B **278**, 417 (1986).
- [41] F. Gliozzi, Nucl. Phys. B **204**, 419 (1982).
- [42] H. Kluberg-Stern, A. Morel, O. Napoly and B. Petersson, Nucl. Phys. B **220**, 447 (1983).
- [43] G. P. Lepage, B. Clark, C. T. H. Davies, K. Hornbostel, P. B. Mackenzie, C. Morningstar and H. Trottier, Nucl. Phys. Proc. Suppl. **106**, 12 (2002) [arXiv:hep-lat/0110175]; C. Morningstar, Nucl. Phys. Proc. Suppl. **109A**, 185 (2002) [arXiv:hep-lat/0112023].
- [44] For a pedagogical introduction see D. S. Sivia, *Data Analysis: A Bayesian Tutorial* (Oxford University Press, USA, 1996); a review can be found in K. Nakamura *et al.* (Particle Data Group), J. Phys. G **37**, 075021 (2010).
- [45] W. M. Yao *et al.* [Particle Data Group], J. Phys. G **33**, 1 (2006) and 2007 partial update for edition 2008 (URL: <http://pdg.lbl.gov>). The 2009-10 updates for the D_s hyperfine splitting have not changed its value. For the B_s hyperfine splitting, the “average value” of 46.1(1.5) has remained consistent; the “fit” value has increased slightly to 49.0(1.5).
- [46] A. S. Kronfeld, Nucl. Phys. B Proc. Suppl. **53**, 401 (1997) [arXiv:hep-lat/9608139].
- [47] E. E. Jenkins, Nucl. Phys. B **412**, 181 (1994) [arXiv:hep-ph/9212295].
- [48] C. M. Arnesen, B. Grinstein, I. Z. Rothstein and I. W. Stewart, Phys. Rev. Lett. **95**, 071802 (2005) [arXiv:hep-ph/0504209].
- [49] E. Eichten and B. R. Hill, Phys. Lett. B **243**, 427 (1990).
- [50] M. Nobes and H. Trottier, PoS **LAT2005**, 209 (2006) [arXiv:hep-lat/0509128]; M. Nobes, “Automated Lattice Perturbation Theory for Improved Quark and Gluon Actions,” (Simon Fraser University) Ph. D. thesis, 2004.
- [51] C. T. Sachrajda and G. Villadoro, Phys. Lett. B **609**, 73 (2005) [arXiv:hep-lat/0411033]; P. F. Bedaque, Phys. Lett. B **593**, 82 (2004)

[arXiv:nucl-th/0402051].

- [52] E. D. Freeland, A. S. Kronfeld, J. N. Simone and R. S. Van de Water [for the Fermilab Lattice and MILC Collaborations], PoS **LAT2006**, 083 (2006) [arXiv:hep-lat/0610108].
- [53] B. Aubert *et al.* [BABAR Collaboration], Phys. Rev. D **74**, 032007 (2006) [arXiv:hep-ex/0604030].
- [54] M. Di Pierro *et al.*, Nucl. Phys. Proc. Suppl. **129**, 328 (2004) [arXiv:hep-lat/0310045].
- [55] V. I. Berestetskii, E. M. Lifshitz, and L. P. Pitaevskii, *Relativistic Quantum Theory* (Pergamon, Oxford, 1971).
- [56] C. Aubin and C. Bernard, Phys. Rev. D **73**, 014515 (2006) [arXiv:hep-lat/0510088].
- [57] C. Aubin and C. Bernard Phys. Rev. D **68** (2003) 034014 [arXiv:hep-lat/0304014].
- [58] C. Aubin and C. Bernard, Phys. Rev. D **68** (2003) 074011 [arXiv:hep-lat/0306026].